Assimilation of Radar Radial Velocity and Reflectivity, Satellite Cloud Water Path, and Total Precipitable Water for Convective-Scale NWP in OSSEs

SIJIE PAN

School of Meteorology, and Cooperate Institute for Mesoscale Meteorological Studies, University of Oklahoma, and NOAA/National Severe Storms Laboratory, Norman, Oklahoma

JIDONG GAO

NOAA/National Severe Storms Laboratory, Norman, Oklahoma

DAVID J. STENSRUD

Department of Meteorology and Atmospheric Science, The Pennsylvania State University, University Park, Pennsylvania

XUGUANG WANG

School of Meteorology, University of Oklahoma, Norman, Oklahoma

THOMAS A. JONES

Cooperative Institute for Mesoscale Meteorological Studies, University of Oklahoma, and NOAA/National Severe Storms Laboratory, Norman, Oklahoma

(Manuscript received 1 May 2017, in final form 15 September 2017)

ABSTRACT

In this study, the ensemble of three-dimensional variational data assimilation (En3DVar) method for convective-scale weather is adopted and evaluated using an idealized supercell storm simulated by the Weather Research and Forecasting (WRF) Model. Synthetic radar radial velocity, reflectivity, satellite-derived cloud water path (CWP), and total precipitable water (TPW) data are produced from the simulated supercell storm and then these data are assimilated into another WRF Model run that starts with no convection. Two types of experiments are performed. The first assimilates radar and satellite CWP data using a perfect storm environment. The second assimilates additional TPW data using a storm environment with dry bias. The first set of experiments indicates that incorporating CWP and radar data into the assimilation leads to a much faster initiation of supercell storms than found using radar data alone. Assimilating CWP data primarily improves the analyses of nonprecipitating hydrometeor variables. The results from the second set of experiments demonstrate the critical importance of the storm environment. When using the biased storm environment, assimilation of CWP and radar data enhances the analyses, but the forecast skill rapidly decreases over the subsequent 1-h forecast. Further experiments show that assimilating the TPW data has a large impact on storm environment that is essential to the accuracy of the storm forecasts. In general, the combination of radar data and satellite data within the En3DVar results in better analyses and forecasts than when only radar data are used, especially for an imperfect storm environment.

1. Introduction

The goal of the NOAA's Warn-on-Forecast (WoF) program is to make more accurate forecasts of high-impact weather events, such as tornadoes, hailstorms, flash floods, and damaging windstorms (Stensrud et al. 2009). To accomplish this goal, high-resolution remote sensing data, such as radar and high-resolution satellite data that provide information on internal storm structures, have to be used. Many studies have demonstrated that effective utilization of high-resolution remote sensing data in convective-scale numerical models leads to significant improvement in severe weather analyses and forecasts (Dowell et al. 2004; Gao and Stensrud 2012;

Corresponding author: Dr. Jidong Gao, jidong.gao@noaa.gov

DOI: 10.1175/JTECH-D-17-0081.1

Gao et al. 2004; Jones and Stensrud 2012; Jones et al. 2013, 2016; Stensrud and Gao 2010; Wheatley et al. 2015; Yussouf et al. 2013; Johnson et al. 2015; Wang and Wang 2017; Johnson and Wang 2017).

Radial velocity and reflectivity from the Weather Surveillance Radar-1988 Doppler (WSR-88D; Crum et al. 1993) can provide important wind and hydrometeor information within areas of precipitation. Assimilating observations from multiple radars was a primary tool used to understand the internal structures and dynamics of convective storms over the past 20 years (Aksoy et al. 2009; Dowell et al. 2011, 2004; Gao and Stensrud 2012; Gao et al. 2004; Sun 2005; Yussouf and Stensrud 2010). For example, Sun (2005) demonstrated the usefulness of radar data in a four-dimensional variational data assimilation (4DVar) system for initializing and forecasting a severe storm. Yussouf and Stensrud (2010) showed the advantages of using the ensemble Kalman filter (EnKF) method to assimilate high-temporal-frequency radar data for convective storms. Despite some encouraging results, a major shortcoming of radar data assimilation remains, in that the assimilation is underdetermined. Only wind and some of the hydrometeor variables are closely related to radar observations, while the other model variables are not directly observed. For instance, nonprecipitating cloud water and ice, which are excluded from commonly used reflectivity operators, may not be properly analyzed in a 3DVar system. Environmental information, such as water vapor content and air temperature, also cannot be captured by the radar observations, yet the environment has a large influence on either the generation or dissipation of convective storms.

The assimilation of satellite data in NWP is very mature on synoptic and mesoalpha scales (Harris and Kelly 2001; Matricardi et al. 2004; Saunders et al. 1999; Vukicevic et al. 2006; Weng 2007; Weng and Liu 2003), with the direct assimilation of satellite radiances being a very common approach. By assimilating radiances, one can avoid the uncertainties and discrepancies in the retrieval algorithms, which differ between instruments (Derber and Wu 1998). However, because of the inaccuracy of radiative transfer models (RTMs) and their sensitivity to the channels being assimilated (Migliorini 2012), satellite radiances are generally assimilated only over clear-sky areas. Although considerable progress in cloudy radiance assimilation has been reported in the past decade (Okamoto et al. 2014; Pavelin et al. 2008; Polkinghorne and Vukicevic 2011; Polkinghorne et al. 2010; Prates et al. 2014; Stengel et al. 2013; Vukicevic et al. 2004; Weisz et al. 2007), applying these methods may introduce additional uncertainties because of different assumptions between the model physics and RTMs, especially at high spatial and temporal resolutions (Zupanski et al. 2011).

One recent application of satellite data for convective-scale NWP is to assimilate derived products from satellite observations, such as cloud water path (CWP). Jones et al. (2013) used CWP retrievals from the Geostationary Operational Environmental Satellite (GOES) to improve hydrometeor mixing ratios over cloudy areas for the severe weather event that occurred on 10 May 2010. In the experiments, both radar data and CWP data were assimilated using the WRF Data Assimilation Research Testbed (DART) program (Anderson et al. 2009) with 40 ensemble members. Results demonstrated that the storm structure was improved and that spurious cells were eliminated, by assimilating CWP data at 15-min intervals over a 3-h data assimilation (DA) period compared to the experiments without CWP assimilation.

With the launch of *GOES-16* (on 19 November 2016), formally known as GOES-R, the application of high-resolution satellite data in convective NWP will be expected to grow rapidly. Both WSR-88D radar observations and *GOES-16* satellite products contain useful information about storm structures and characteristics. In addition, *GOES-16* products, such as total precipitable water (TPW) data, contain water vapor information, which is an important component of the storm environment.

The environment in which convection develops can be as important to the forecast as the details of the convection itself and thus it is highly beneficial to create a good initial condition for severe weather prediction. Kuo et al. (1996) conducted a set of experiments indicating that even when using a first guess with a very poor initial moisture field, 4DVar was quite effective in improving the vertical moisture distribution when TPW was assimilated. But this study was conducted at only mesoscale resolutions. For convective-scale NWP, the importance of the storm moisture environment has not been extensively studied. Thus, we study the impact of assimilating CWP and TPW (both of which will be *GOES-16* products) on the analysis and forecast of an idealized supercell storm together with the assimilation of radar data using the En3DVar method (Gao et al. 2016).

A concept of the ensemble of DAs (EDA) used by Météo-France and ECMWF (Berre et al. 2007; Bonavita et al. 2012) was adopted in Gao et al. (2016). The only difference between the operational approaches is that Gao et al. used extended control variables, or so-called alpha control variables (Lorenc 2003; Wang et al. 2008), for introducing ensemble covariances into the variational system. The EDA approach would be very

expensive if 4DVar is used as the core DA scheme, so the En3DVar uses 3DVar as its core DA scheme. This choice takes advantage of both the ensemble assimilation technique and 3DVar, since flow-dependent background error covariances estimated from an ensemble forecast are used, as multivariate correlations are more conveniently modeled by ensemble covariances, while the computationally high efficiency of 3DVar method is retained. Once this is completed, two groups of experiments are performed. The first group assimilates radar and satellite CWP data using a perfect storm environment, similar to that described in Jones et al. (2013), but using the En3DVar framework. The second group assimilates TPW data in addition to radar and satellite CWP data, as a storm environment with dry bias is used. The motivation for these two scenarios is to examine to what extent the recently launched *GOES-16* produced CWP and TPW products can benefit convective-scale data assimilation and NWP beyond the benefits already provided from radar data assimilation.

The methodology of the En3DVar scheme used for assimilating radar and satellite data is briefly described in section 2. Section 3 provides an introduction of the model configurations, the forward operators for the observations, and the experimental design. The diagnostics of the analyses are addressed in section 4. Section 5 qualitatively and quantitatively verifies the forecast performance. Conclusions are given in section 6.

2. Methodology

The En3DVar method adopted in this study was used by Gao et al. (2016). The basic concept of En3DVar method is to minimize the cost function J_k, where k is the number of ensemble members, defined as the background term and the observation term plus other constraint terms:

$$J_k = \frac{1}{2}(\mathbf{x}_k - \mathbf{x}_k^b)^{\mathrm{T}}\mathbf{B}_e^{-1}(\mathbf{x}_k - \mathbf{x}_k^b) + \frac{1}{2}[H(\mathbf{x}_k) - \mathbf{y}_k^o]^{\mathrm{T}}\mathbf{R}^{-1}[H(\mathbf{x}_k) - \mathbf{y}_k^o] + J_c(\mathbf{x}_k) \quad (1)$$

where $\mathbf{x}_k$ and $\mathbf{x}_k^b$ are the analysis and background state vectors for ensemble member k, respectively; $H(\mathbf{x}_k)$ is the observation operator; and $\mathbf{y}_k^o$ are the observation vectors. Random perturbations are applied to the original observation to generate various observations for each ensemble member, similar to the stochastic EnKF (Houtekamer and Mitchell 1998). The constraint term J_c could contain any dynamical equation as a weak constraint, for example, a momentum equation for radar radial velocity used by Xu et al. (2001) and Xu and Wei (2013). In this study, the mass continuity equation is introduced into the penalty term J_c as a weak constraint. Details relating to this constraint term were discussed by Gao et al. (2016). Terms $\mathbf{B}_e$ and $\mathbf{R}$ are the background and observation error covariance matrices, respectively. Following Derber and Rosati (1989) and Courtier (1997), define an alternative control variable $\mathbf{v}$ that makes an optimal analysis increment $\Delta\mathbf{x}_k = (\mathbf{x}_k - \mathbf{x}_k^b) = \mathbf{B}_e^{1/2}\mathbf{v}_k$. Then the cost function can be written in a preconditioned incremental form,

$$J_k = \frac{1}{2}\mathbf{v}_k^{\mathrm{T}}\mathbf{v}_k + \frac{1}{2}[H(\mathbf{x}_k^b + \mathbf{B}_e^{1/2}\mathbf{v}_k) - \mathbf{y}_k^o]^{\mathrm{T}} \times \mathbf{R}^{-1}[H(\mathbf{x}_k^b + \mathbf{B}_e^{1/2}\mathbf{v}_k) - \mathbf{y}_k^o] + J_c(\mathbf{v}_k). \quad (2)$$

The background error covariance $\mathbf{B}_e$ in the traditional 3DVar scheme is static and does not reflect the flow dependency of error growth that relies on the particular atmospheric situation. An essential difference of En3DVar from the 3DVar framework is that the flow-dependent covariance $\mathbf{B}_e$ is derived from an ensemble of forecasts and establishes correlations between different model variables.

In our experiments, an ensemble of En3DVar analyses and an extra control member were performed simultaneously by minimizing the cost function [(2)] to update the analysis variables. The ensemble covariance used in the En3DVar analysis for each ensemble member is derived from the other ensemble forecasts except itself. For the control member, the covariance is estimated from the entire ensemble forecasts. Then the ensemble analyses were centered on the control analysis and inflated using the statistical information from the ensemble backgrounds and analyses. The inflation process is applied on each grid point according to the equation

$$\mathbf{x}_k^a = \mathbf{x}_c^a + \gamma(\mathbf{x}_k^a - \overline{\mathbf{x}^a}) + (1-\gamma)(\mathbf{x}_k^b - \overline{\mathbf{x}^b}), \quad (3)$$

where $\mathbf{x}_c^a$ is the analysis of the control member, $\mathbf{x}_k^a - \overline{\mathbf{x}^a}$ indicates the perturbation from the mean of ensemble analyses, and $\mathbf{x}_k^b - \overline{\mathbf{x}^b}$ denotes the perturbation with respect to the mean of ensemble background forecasts. The γ is set to 0.5 in this case such that the new analysis perturbations are calculated by mixing half of analysis and half of original background perturbations (Zhang et al. 2004). The ensemble analyses after inflation can be considered as the initial conditions for the next step. Once the control analysis and the initial conditions of ensemble members are prepared, 5-min forecasts are started and then a DA cycle is finished. The above-mentioned operations are repeated several times depending on the number of DA cycles.

Closely following Gao et al. (2013) and Gao and Stensrud (2014), both radial velocity and reflectivity are always assimilated in this study. The CWP and TPW data are incorporated into the DA process to evaluate the impact of these satellite-derived data. The forward operators for radial velocity and reflectivity are chosen from Gao and Stensrud (2012). Work by Chen et al. (2015) is adopted for converting model variables to CWP. For computing TPW, a derivation defined by the theoretical basis document for the *GOES-16* Advanced Baseline Imager (ABI) is used in our analysis system. Forward operators introduced here are briefly discussed in the next section.

Analysis variables include the three-dimensional wind fields u, v, and w; potential temperature θ; air pressure p; water vapor mixing ratio q_v; and the hydrometeors that depend on the microphysics scheme, usually containing cloud water mixing ratio q_c, rainwater mixing ratio q_r, ice mixing ratio q_i, snow mixing ratio q_s, and graupel mixing ratio q_g. Because the WRF Model requires the geopotential ϕ and mass of dry air μ as prognostic variables instead of pressure p, to better initialize the WRF Model, the geopotential and dry air mass are calculated so that the updated variables exactly match the prognostic variable of the WRF Model.

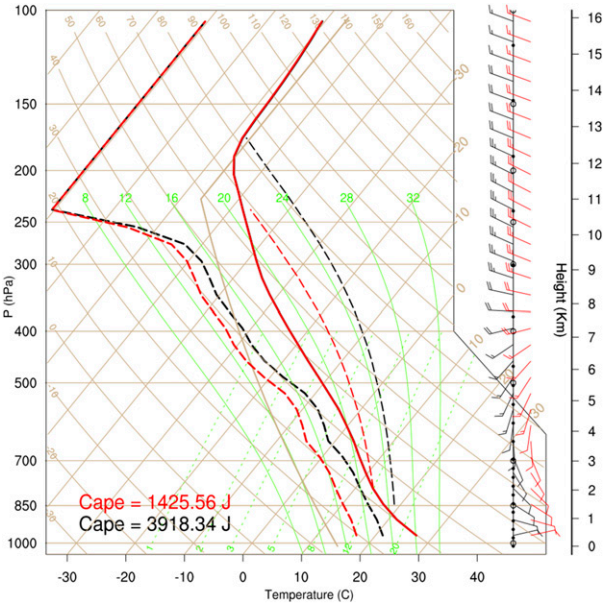

FIG. 1. Slightly modified sounding of a classic supercell event that occurred on 20 May 1977 in Del City for the truth simulation (black), the first set of experiments (black), and second set of experiments (red), including temperature (solid line), dewpoint temperature (thick dashed line), and CAPE (thin dashed line).

3. Experimental design and forward operator

a. *Model configuration and truth simulation for OSSE*

To test the En3DVar approach, a fully compressible, nonhydrostatic Advanced Research version of the Weather Research and Forecasting (WRF-ARW) Model, version 3.6.1, was used in a three-dimensional idealized mode for a quarter-circle shear supercell simulation. The horizontal spatial resolution is 1 km with 80 points in the north–south and east–west directions, while 40 stretched eta vertical levels up to 20 km above ground level (AGL; approximately 50 hPa) were chosen so that the distance between each vertical level has a nearly constant value. Open lateral boundary conditions and Rayleigh damping for the top boundaries were used for this idealized case. The length of the simulation extends to 2 h.

The simulation was initialized with a slightly modified sounding (Fig. 1, black line) of a classic supercell event that occurred on 20 May 1977 in Del City, Oklahoma. Similar to the past studies (Adlerman and Droegemeier 2002; Noda and Niino 2003; Rotunno and Klemp 1985; Weisman and Klemp 1982), an ellipsoidal thermal bubble was added in truth simulations to trigger convection. The warm bubble had a potential temperature perturbation of 3 K at the location $x = 60$ km, $y = 25$ km, $z = 1.5$ km with a 10-km horizontal radius and a 1.5-km vertical radius. The Thompson scheme, a single-moment 5-class microphysics scheme containing the predicted number concentration of ice and rain, was used to depict the microphysical processes. The turbulence parameterization scheme was the standard 1.5-order TKE closure. Cloud and radiation physics were not applied in this idealized simulation.

During the truth simulation started from the warm bubble, the initial convection intensifies in the first 30 min (Figs. 2a–d) accompanied by the cloud forming around 10 min (Fig. 3a). Rainwater appears at 15 min (Fig. 3b), while ice hydrometeors are generated at 20 min (Figs. 3c–e). The storm keeps developing and reaches its strongest intensity at 40 min (Figs. 2e,f) and then it starts to split (Fig. 2g), accompanied by a slight decrease in intensity. The right-splitting cell (which stays at the center of the domain) tends to control the system after this point, as indicated by a warm core in the midtroposphere, the cold pool near the surface, the classical characteristic of a "hook echo," and an updraft reaching a maximum value 64 m s^{-1} around 10 km AGL at 75 min.

b. *Synthetic radar observations*

The synthetic radar data are sampled from the truth simulation using the appropriate volume coverage

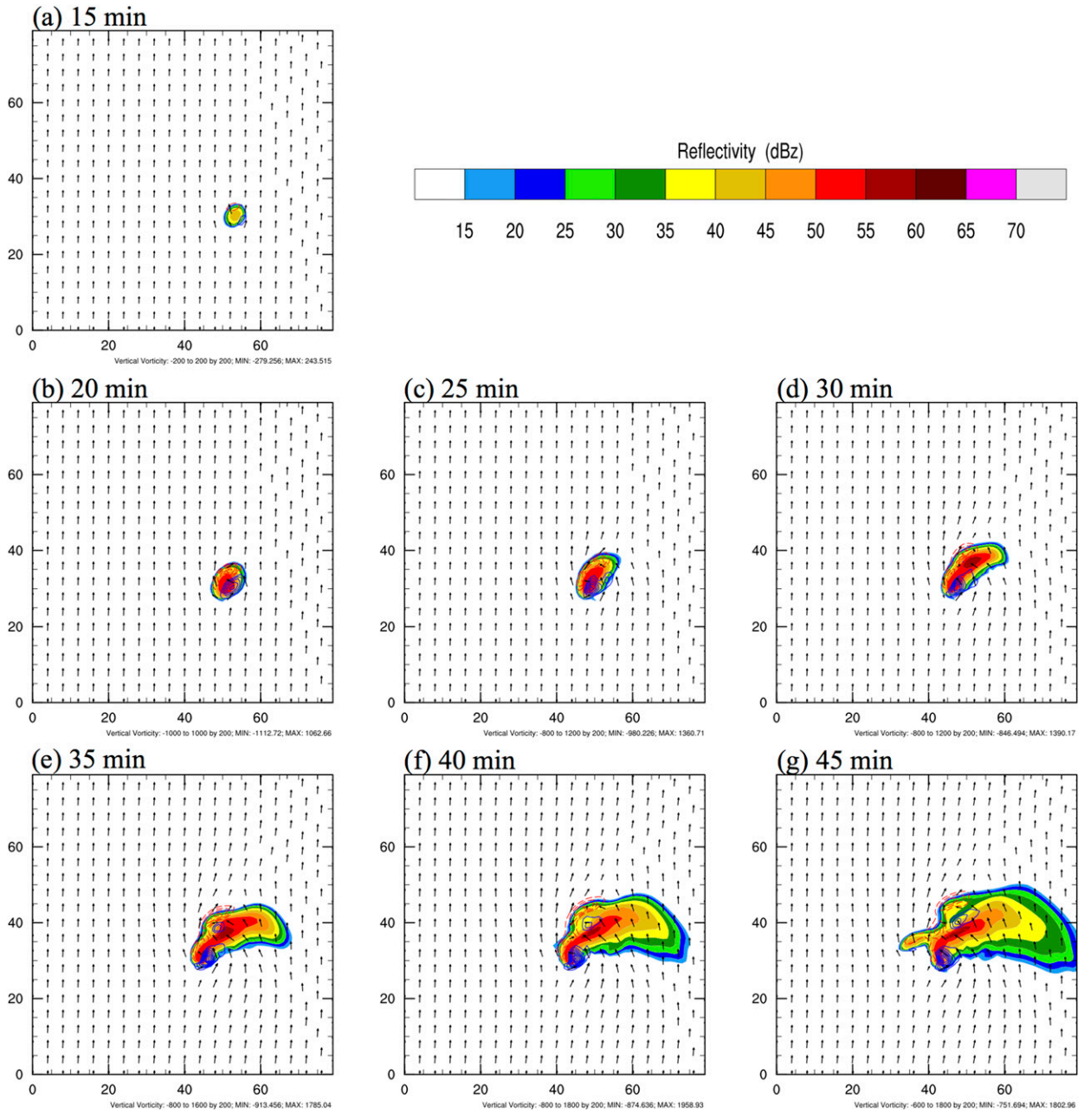

FIG. 2. Simulated reflectivity (dBZ, shaded), wind field (m s^{-1}, arrows), and relative vorticity (10^{-5} s^{-1}, contours) at 4 km AGL from 15 to 45 min as the reference truth. Positive vorticities (blue solid lines) and negative vorticities (red dashed lines) are indicated.

pattern (VCP), which is based on the type of weather occurring. Corresponding to the operational WSR-88D scanning strategy, radial velocity and reflectivity are calculated on 14 different elevation angles for the deep convection mode. Available radar observations are located on model grid points. Synthetic radar observations are determined for two radar locations, placed at the southwest and northeast corners of the domain, respectively.

The synthetic radial velocity is defined using the following equation:

$$V_r = u\sin\phi\cos\mu + v\cos\phi\cos\mu + w\sin\mu, \qquad (4)$$

where (u, v, w) are the wind components from the model forecast on staggered grid points, μ is the elevation angle, and ϕ is the azimuthal angle of radar beam.

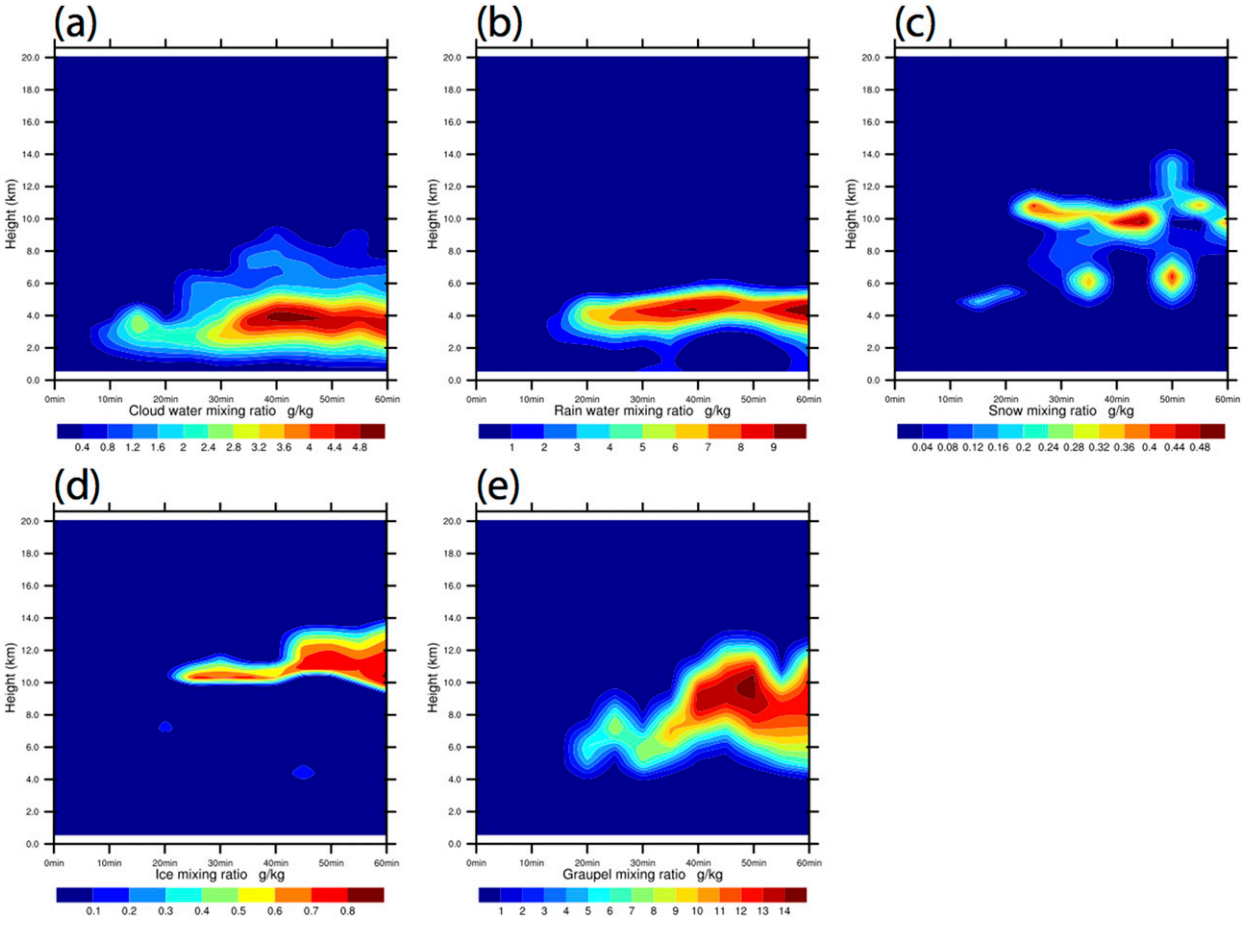

FIG. 3. Time–height composites of maximum hydrometeor mixing ratios (g kg^{-1}) for the truth simulation. (a) Cloud water, (b) rainwater, (c) snow, (d) ice, and (e) graupel.

The forward model for calculating synthetic reflectivity is based on Smith et al. (1975) and Schoenberg Ferrier (1994). Following Gao and Stensrud (2014) and Gao et al. (2016), the radar reflectivity factor is obtained by gathering the rainwater, snow, and graupel mixing ratio,

$$Z_e = Z(q_r) + Z(q_s) + Z(q_g), \quad (5)$$

$$Z_{\mathrm{dB}} = 10 \log_{10} Z_e. \quad (6)$$

Once synthetic radar observations are generated, reflectivities that are less than 15 dBZ are set to be zero and considered as precipitation-free regions. Then random perturbations are added to the synthetic radar observations over precipitating areas for all members except the control. Normally distributed errors with zero mean and a standard deviation of 2 m s^{-1} are added to the synthetic radial velocity on each available grid point. For reflectivity, the errors also have a Gaussian distribution with zero mean but with a standard deviation of 10 dBZ and are added to the synthetic reflectivity on grid points where the reflectivity is greater than the threshold value of 15 dBZ. The same set of observation perturbations is used in all experiments.

c. *Synthetic satellite observations*

Satellite data are a potential resource for storm-scale data assimilation, as they have wider spatial coverage than radar and fill many of the gaps seen when using only radar observations. Two types of satellite retrieval data are prepared for this study. CWP is the column amount of liquid and frozen water (kg m^{-2}) in the cloud. It represents the horizontal distribution and weight of the liquid and ice hydrometeors in the atmosphere. For clear sky, the CWP is 0 kg m^{-2}. As the concentration of liquid water or ice in a cloud goes up, so does the value of CWP. However, since CWP is a vertically integrated quantity, it cannot capture the vertical distribution of cloud water. Yet information

TABLE 1. Assimilation experiments with different types within each sounding.

	Soundings	Experiments	Radial velocity + reflectivity	CWP	TPW
Set 1	Original sounding	RAD1	√		
		RADCWP1	√	√	
Set 2	Less moisture sounding	RAD2	√		
		RADCWP2	√	√	
		RADSAT	√	√	√

provided by CWP is still helpful for improving the analysis of the nonprecipitating hydrometeor variables that are not seen in reflectivity observations. Besides CWP, cloud-base heights, cloud-top heights, and cloud phases are additionally offered in several real-time retrieval algorithms (Minnis et al. 2008a,b, 2011).

Synthetic CWPs are created by integrating the hydrometeor variables from the truth simulation in atmospheric columns. First, the cloud water mixing ratio and ice mixing ratio are summed to compute the total cloud water mixing ratio at each grid point. Then the CWP is obtained by accumulating the total water mixing ratio from the cloud base to cloud top using the following formula:

$$\mathrm{CWP} = \frac{1}{g}\int_{\mathrm{CBP}}^{\mathrm{CTP}} [q_c(p) + q_i(p)]\, dp, \tag{7}$$

where q_c and q_i are the cloud water and ice mixing ratios, respectively; g is the gravity acceleration; and p is the air pressure on the model level. Cloud-base pressure (CBP) is chosen by finding the LCL, and cloud-top pressure (CTP) is defined by locating the pressure where the liquid water and ice mixing ratio are less than $10^{-3}\,\mathrm{g\,kg^{-1}}$. While observed CWP includes the contribution from precipitating hydrometeors (i.e., q_r, q_s, and q_g), for the purposes of this work the CWP experiments assimilate only CWP in mostly precipitation-free regions. A threshold of 15 dBZ was set to distinguish precipitating areas from nonprecipitating areas. In other words, CWP data are assimilated only where reflectivity is less than 15 dBZ if radar data are applicable. The standard deviation for CWP is set to $100\,\mathrm{g\,m^{-2}}$.

TPW is the amount of liquid water (cm) that would be produced if all the atmospheric water vapor in a vertical column were condensed. To keep consistency between the algorithm of synthetic TPW and the method for GOES-R ABI (Li et al. 2010), only water vapor between the surface and 300 hPa is accumulated to derive TPW because of the negligible water vapor content above 300 hPa. All five classes of hydrometeor variables plus the water vapor mixing ratio will be directly updated by using synthetic radar reflectivity and satellite retrieval data during DA cycles. For synthetic TPW data, the algorithm defined in the *GOES-16* ABI document is used. Only the water vapor mixing ratio is required, which is defined as

$$\mathrm{TPW} = \frac{1}{\rho_w g}\int_{p_s}^{300\,\mathrm{hPa}} q_v(p)\, dp. \tag{8}$$

In this equation, ρ_w is the water density of $1000\,\mathrm{kg\,m^{-3}}$, p_s is the surface pressure (hPa), and q_v is the water vapor mixing ratio. Otherwise, the calculation is similar to that used for CWP. The standard deviation for TPW is set to 5 mm.

d. Experimental design

We performed two sets of experiments (Table 1) with backgrounds started from different environmental soundings. Both experiments use the same procedure to examine the impact of various datasets. The first set of DA experiments is initialized using the identical sounding as used in the truth simulation but without introducing an ellipsoidal thermal bubble (so that without assimilating radar and satellite data, the storm never develops). The second set of experiments uses a sounding with a dry bias (Fig. 1, red line) to define the storm environment. In both experiments, the ensemble size is set to 50. To generate the initial ensemble members, perturbations are added to the horizontally homogeneous backgrounds for both experimental groups. The random perturbation has a normal distribution with zero mean and a standard deviation of $5\,\mathrm{m\,s^{-1}}$ for horizontal wind, $3\,\mathrm{m\,s^{-1}}$ for vertical wind, 3 K for potential temperature, and an appropriate deviation dependent on model levels for the water vapor mixing ratio. Once the random perturbations are generated, a three-dimensional recursive filter is applied to smooth the random perturbations. The method closely follows that used in Gao and Stensrud (2014). Perturbations are added over the whole domain except for the five points closest to the boundaries. No perturbations for the hydrometeor, the mass of dry air, or the geopotential are included at the initial time. A 15-min ensemble forecast is launched thereafter so that the random perturbations grow dynamically, leading to a larger ensemble spread that has a more reasonable covariance structure than found by perturbing the initial sounding only.

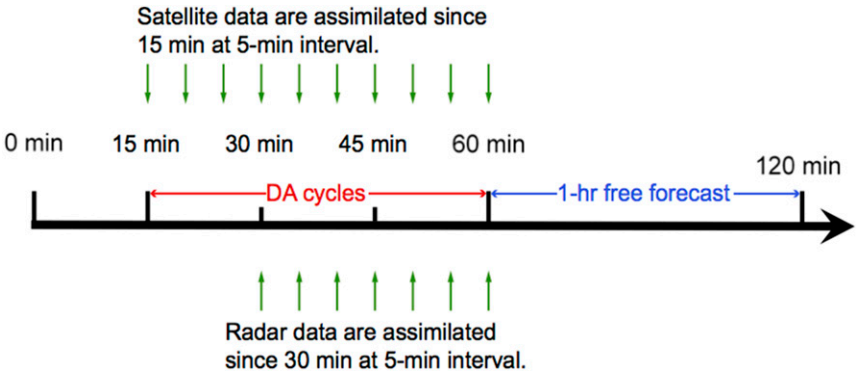

FIG. 4. Time series flowchart of radar and satellite data assimilation cycles for the experiments listed in Table 1.

In both sets of experiments, satellite data are assimilated at 5-min intervals beginning 15 min prior to the start of radar data assimilation. Radar data with or without satellite data are assimilated every 5 min. This 5-min assimilation–forecast cycle is repeated until 60 min of model integration time is reached. In all experiments, the correlation scale is 4 km in the horizontal and 1 km in the vertical for the first outer loop and 2 km in horizontal and 1 km in vertical for the second outer loop. The RAD1 and RAD2 experiments assimilate only radial velocity and reflectivity, identifying the performance of radar DA under different situations of the atmosphere (RAD1 uses the truth sounding, RAD2 uses the dry biased sounding). The RADCWP1 and RADCWP2 experiments assimilate CWP data in addition to radar data using the two environmental soundings. The final RADSAT experiments combines radar and all satellite data to determine whether the TPW data have a positive impact when the dry biased storm environment is used compared to using radar data or CWP data only. Because the storm environment was set to perfect in the first set of experiments, there is no need to assimilate TPW data. While Jones et al. (2015) have demonstrated the effectiveness of clear-sky CWP observations for suppressing spurious cells, in our experiments both zero reflectivity and clear-sky CWP are assimilated to inhibit the development of spurious convections in all experiments. After the 30-min assimilation of radar data (or 45 min of satellite data assimilation if applied), a 1-h free forecast is launched with the control member and the results are compared to the truth simulation to evaluate forecast performance (Fig. 4).

4. Analysis diagnostics

a. Experiments with perfect storm environment

To inspect the performance of the DA results, the analyses of the control member are shown for each experiment after seven DA cycles of radar data, and 10 cycles of CWP data if they are assimilated (at 60 min of model time). Comparing the analysis with the truth simulation at 4 km AGL in Fig. 5a, both RAD1 (Fig. 5c) and RADCWP1 (Fig. 5e) recover most of the storm characteristics, such as the strong reflectivity core and midlevel mesocyclone. Almost all areas of $> 50\,\mathrm{dBZ}$ reflectivity within the right-splitting storm are well recovered in the analysis. Stronger convergence is shown in RADCWP1 with a maximum vorticity of $1431 \times 10^{-5}\,\mathrm{s}^{-1}$ (Fig. 5e), which is close to the $1640 \times 10^{-5}\,\mathrm{s}^{-1}$ value found in the truth run (Fig. 5a). Vertical cross sections of reflectivity are also created along a line 35 km from the southern boundary where the maximum vertical velocity is located in the truth simulation. The patterns of reflectivity and vorticity shown in the vertical section for RADCWP1 (Fig. 5f) represent the true state of the atmosphere better near the tropopause (about 10 km). The vorticity structure of the main storm and the reflectivity core around $x = 35\,\mathrm{km}$ are much more organized and consistent with the truth if additional CWP data are assimilated (Fig. 5f). Spurious echoes in low and midlevels around the major cell are also effectively eliminated.

The vertical distribution of hydrometeor mixing ratios supplies extra information. Each experiment generates broadly similar properties of the hydrometeor fields compared to truth, but each experiment also reveals differences in detail. All experiments more or less decrease the maximum concentrations of the precipitating hydrometeors (rain, snow, graupel; Figs. 6f–h,k–m vs Figs. 6a–c), with a smaller amount of decreasing in RADCWP1. This result indicates that assimilating CWP data in addition to radar data provides a better representation of the precipitating hydrometeors. Furthermore, without assimilated CWP data, nonprecipitating hydrometeors (cloud water and ice; Figs. 6i,j) are noticeably less than those present in the reference truth.

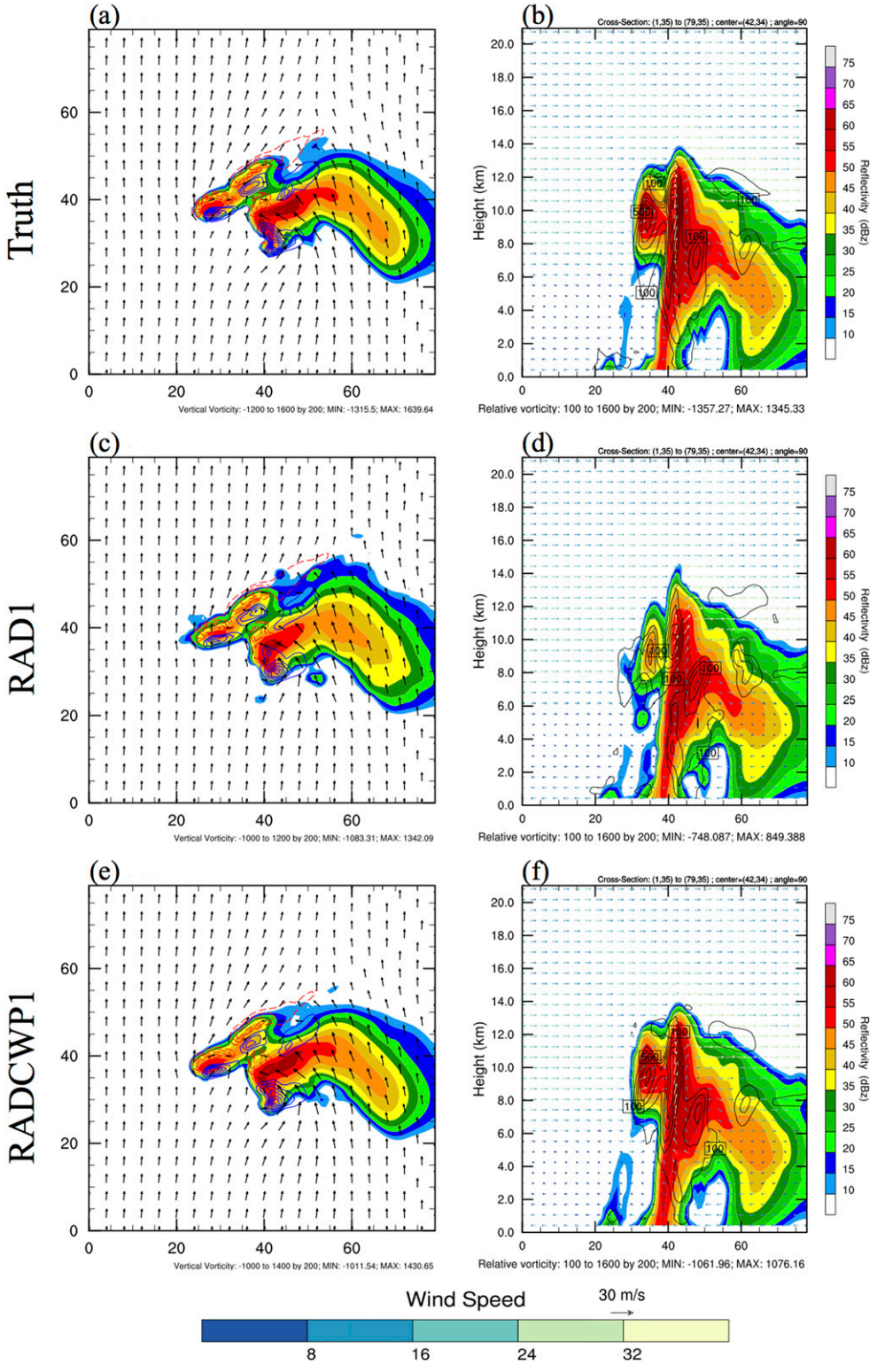

FIG. 5. Wind vectors, reflectivity, and vorticity in (a),(c),(e) horizontal cross section at 4 km AGL and (b),(d),(f) vertical cross section at $y = 35$ km for the truth simulation, RAD1, and RADCWP1 at 60 min.

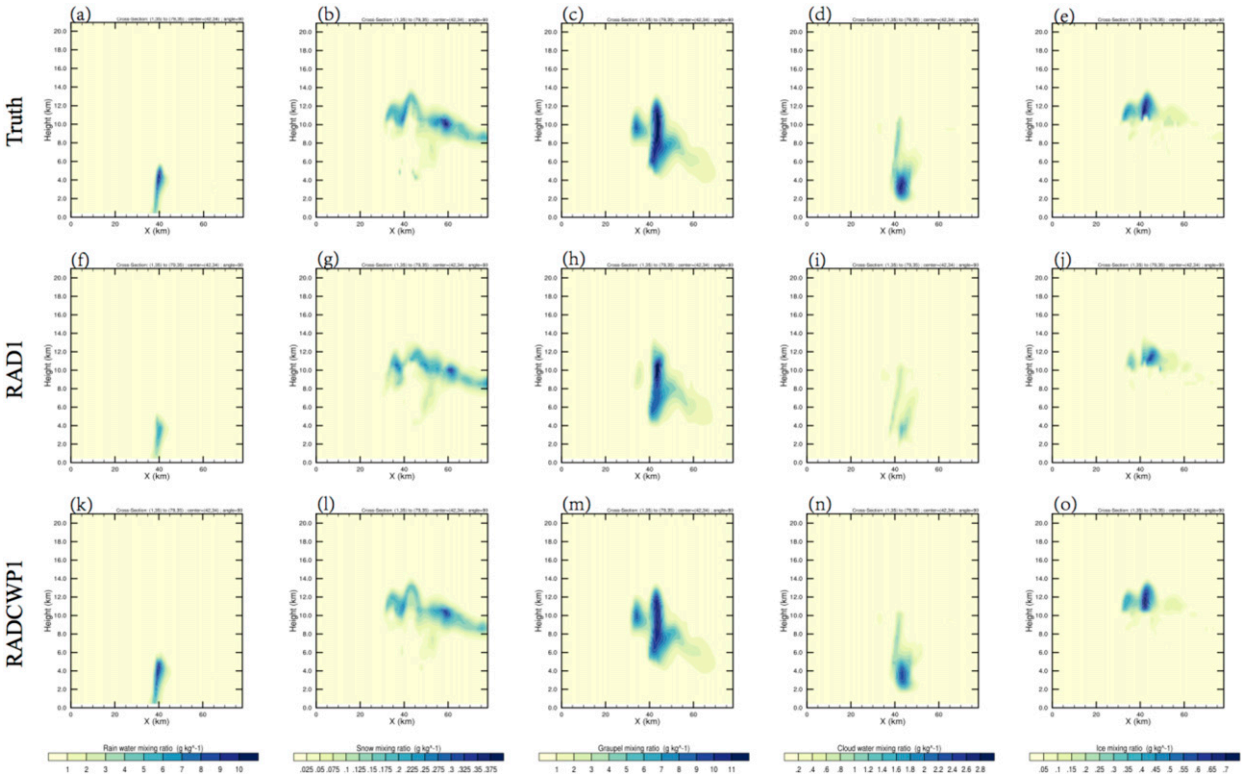

FIG. 6. Vertical cross section of five hydrometeor mixing ratios, including (a),(f),(k) rainwater, (b),(g),(l) snow, (c),(h),(m) graupel, (d),(i),(n) cloud water, and (e),(j),(o) ice across $y = 35$ km for truth, RAD1, and RADCWP1 at 60 min.

The mixing ratio of cloud water analyzed in RADCWP1 (Figs. 6n,o) is $>2.2\,\mathrm{g\,kg^{-1}}$ with an ice mixing ratio $> 0.7\,\mathrm{g\,kg^{-1}}$—values that are much closer to the truth run (Figs. 6d,e) than the experiment RAD1. The coverage of cloud water $> 1.6\,\mathrm{g\,kg^{-1}}$ and cloud ice $> 0.5\,\mathrm{g\,kg^{-1}}$ in RADCWP1 is comparable to the truth. These results suggest that assimilating CWP data accelerates the initialization of both precipitating and nonprecipitating hydrometeor variables.

The root-mean-square errors (RMSE) with and without assimilating CWP data compared with the truth simulation during the DA cycles are shown in Fig. 7. The statistics are calculated over the area where observed reflectivity is greater than the threshold 15 dBZ. Sawtooth patterns in RMSE are usually present wildly for variables directly related to observations, for example, u and w. In contrast with the RMSE for variables not directly observed by radar, or CWP—for example, potential temperature—sawtooth patterns are discernable but not wildly. This occurs because during the analysis step, the variables directly related to observations incur a larger decrease (constrained directly by the observations). Then during the 5-min forecast step, the errors for these variables grow faster than the errors in those variables not directly related to the observations in the analysis step (Gao and Stensrud 2014). Within the first 10 min of the DA cycles (15–25 min), assimilating only CWP data increases the RMSE of the selected variables because CWP data do not have enough information to initialize the convection in such a short period. After the steep increment, the RMSEs start decreasing with the cycles moving forward. Once the radar data are assimilated, these RMSEs rapidly decrease in 10 min. At the end of the DA cycles, the errors are smaller than those in RAD1 by at least a factor of 3.

Since we usually have cloud signal from satellite before available radar precipitation observations (Jones and Stensrud 2012; Jones et al. 2013), we choose to assimilate satellite data prior to radar assimilation in our experiments. But to further investigate whether the improvements are due to the earlier availability of satellite observations or additional observation types, an extra experiment that assimilates both data beginning at the same time (30 min of model integration time) has been performed as well. Based on the statistics (Fig. 7, blue lines), additional CWP data have advantages on the analyses after three assimilation cycles when both radar and satellite data assimilations begin at the same time. However, earlier availability of satellite observations has a much bigger positive impact and accelerates the

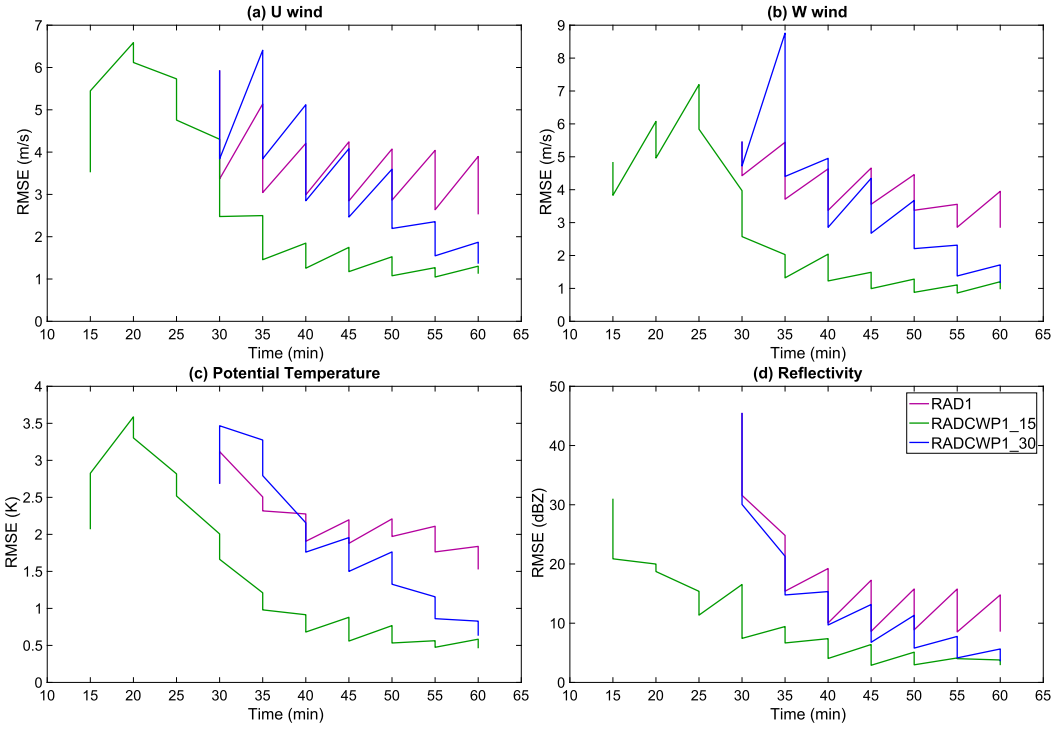

FIG. 7. RMSE of the En3DVar analysis and forecast for the RAD1 (purple) and RADCWP1 (green) experiments, and an extra experiment (blue) that is similar to RAD1 but uses both radar and CWP data. (a) u ($\mathrm{m\,s^{-1}}$), (b) w ($\mathrm{m\,s^{-1}}$), (c) perturbation pt (K), and (d) simulated rf (dBZ).

speed of RMSE convergence. The result suggests that both an additional type of and earlier availability of CWP observations have positive impacts and lead to the improvement of the analyses.

In summary, the storm patterns are approximately recovered in these two experiments. But large improvements are emphasized in the RADCWP1 experiment based on the statistics. The qualitative and quantitative analyses, including differences in hydrometeor variables between the experiments and the truth, and the steeper decrease of RMSEs, demonstrate a faster spinup time and better analyses when additional CWP data are assimilated. However, like many previous OSSEs for convective-scale DA, all the abovementioned experiments are done in a perfect storm environment, which is not realistic.

b. *Experiments with dry bias in storm environment*

The impacts of radar data and satellite retrievals in the En3DVar analysis are evaluated by another set of experiments using a modified sounding with a dry bias. The temperature profile is identical to that in the original sounding but the dewpoint temperature is decreased, since the water vapor content is artificially reduced by 15% for all layers. In this way, the CAPE for the new sounding (Fig. 1, red lines) decreases to $1426\,\mathrm{J\,kg^{-1}}$ (from $3918\,\mathrm{J\,kg^{-1}}$ in the truth run) as a result of the reduced moisture in the lower troposphere. The environment for this case is unable to sustain deep convection when started with a thermal bubble (not shown). Figure 8 depicts wind vectors and reflectivity in both horizontal and vertical cross sections at the end of each assimilation cycle, with the vertical cross sections taken across $y = 35\,\mathrm{km}$. The horizontal wind analyses for all experiments look very good, because radial velocities are directly assimilated. But when we compare the vorticity or reflectivity patterns, the experiments with different observation sources result in totally different analyses. RAD2 almost fails in producing two supercells (Fig. 8a), where the maximum value of the reflectivity for the left-moving cell is less than 35 dBZ compared to 55 dBZ in the truth run (Fig. 5a). Meanwhile, the strong vorticity of $1640 \times 10^{-5}\,\mathrm{s^{-1}}$ associated with reflectivity > 55 dBZ within the right-splitting cell in the truth run is not seen in RAD2. Comparing Fig. 8b with Fig. 5a, we find that the analysis with only radar data does not recover the rising motions in either the upper levels (10–13 km AGL) or the lower levels (2–4 km AGL), and the corresponding narrow area of high reflectivity from the surface to 14 km above the ground

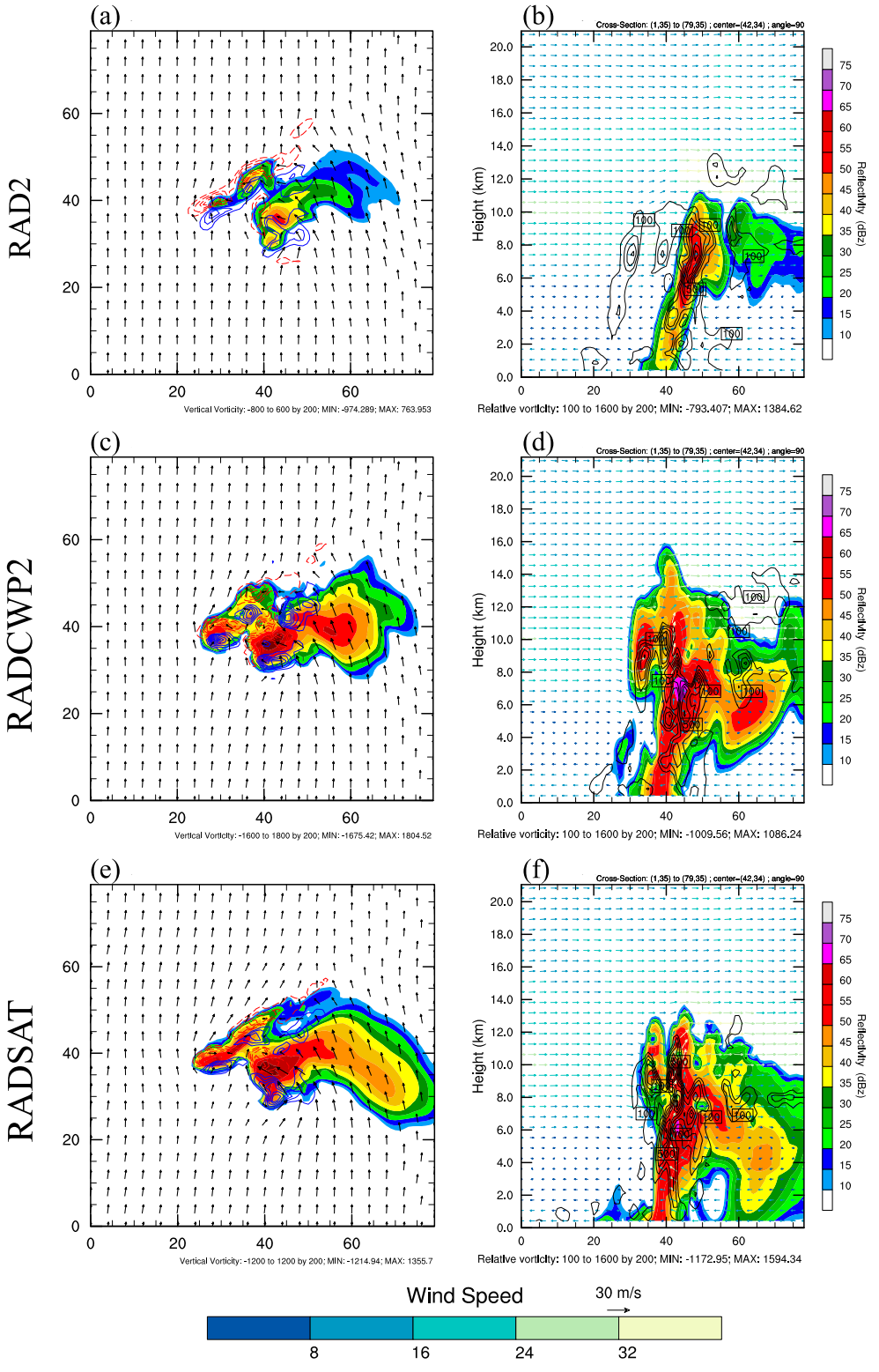

FIG. 8. As in Fig. 5, but for experiments RAD2, RACWP2, and RADSAT.

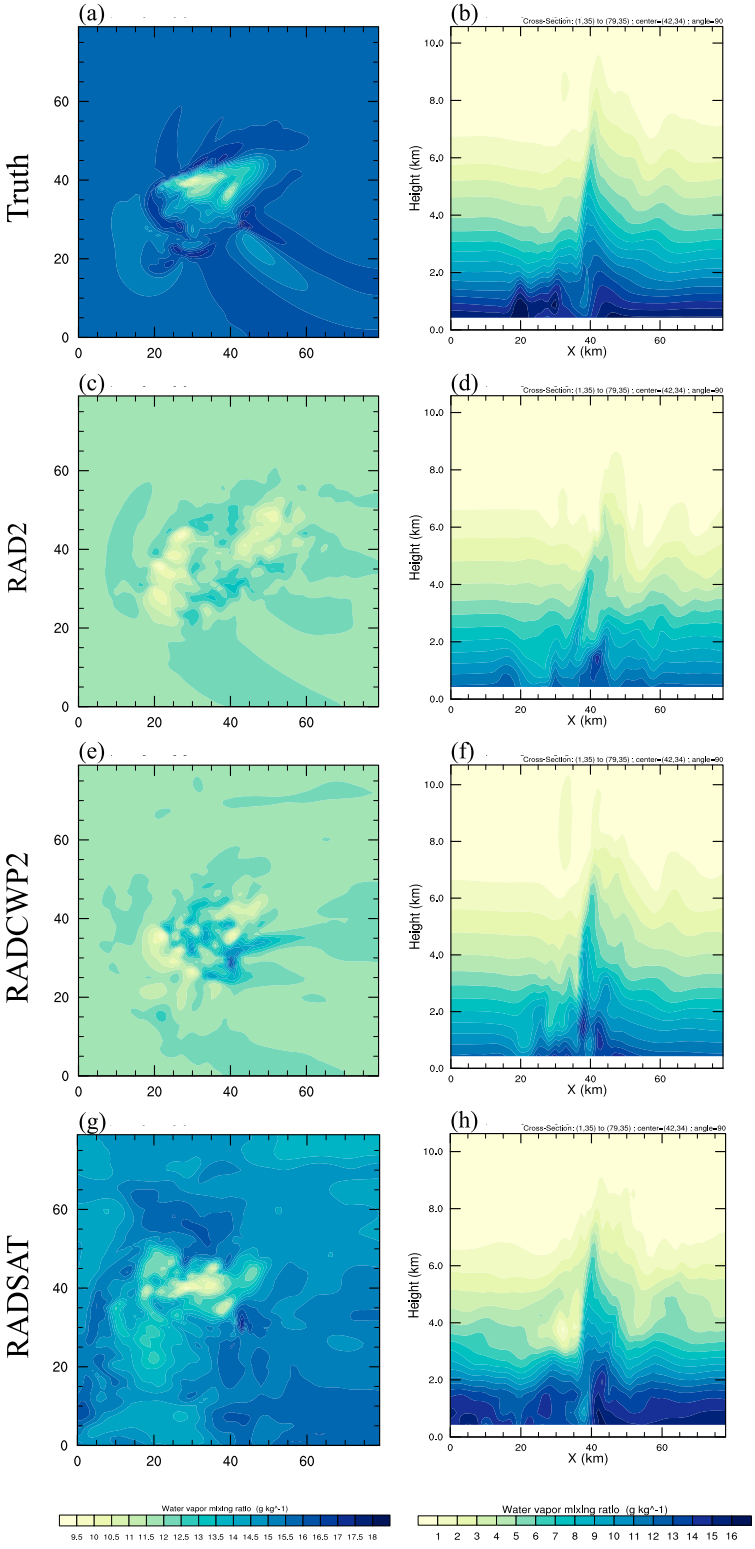

FIG. 9. Water vapor mixing ratio in the (a),(c),(e),(g) horizontal cross section at 500 m AGL and (b),(d),(f),(h) vertical cross section at $y = 35$ km for truth, RAD2, RADCWP2, and RADSAT at 60 min.

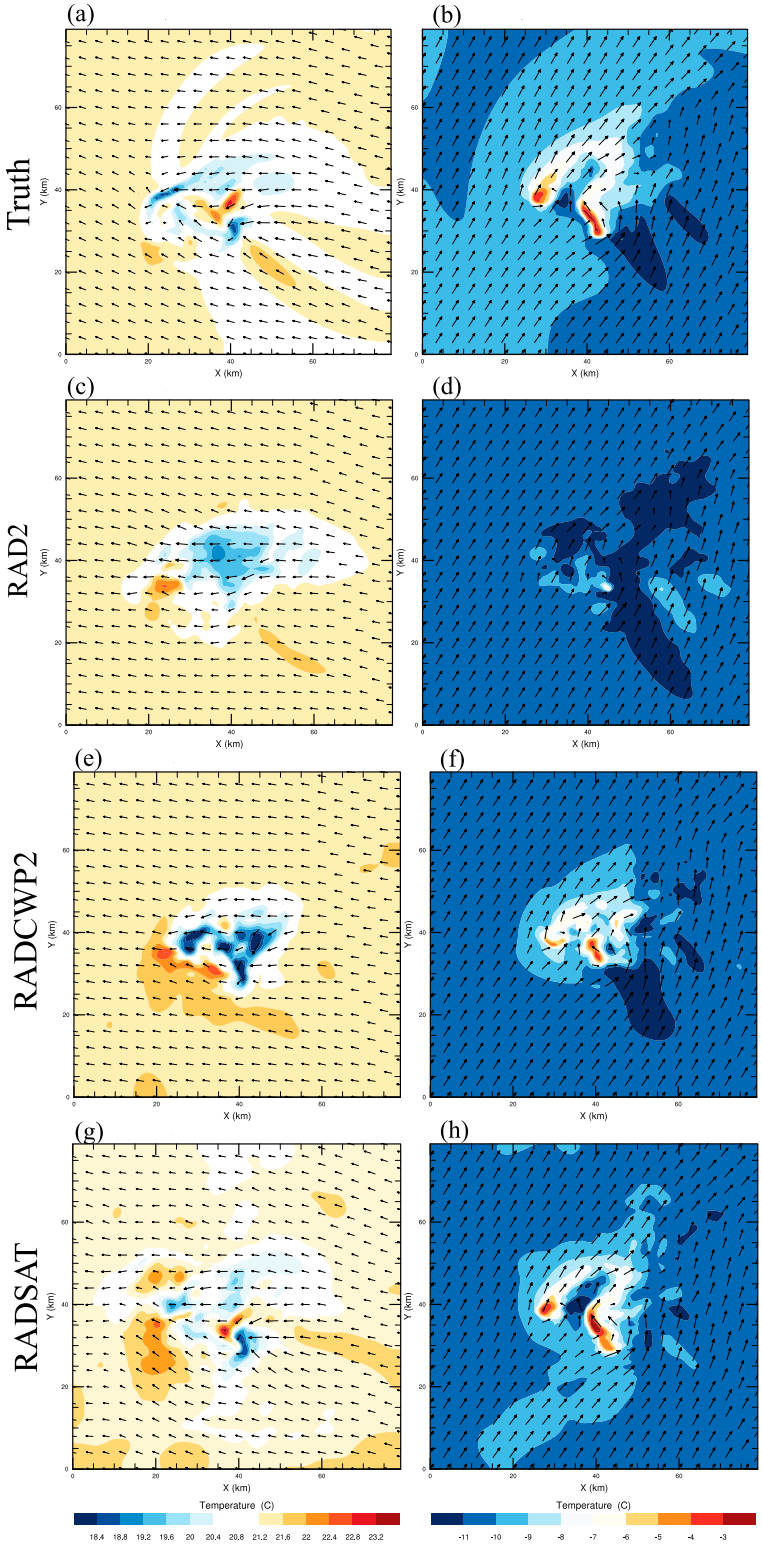

FIG. 10. Temperature and wind fields at (a),(c),(e),(g) 900 and (b),(d),(f),(h) 500 hPa for the truth simulation, and experiments RAD2, RADCWP2, and RADSAT.

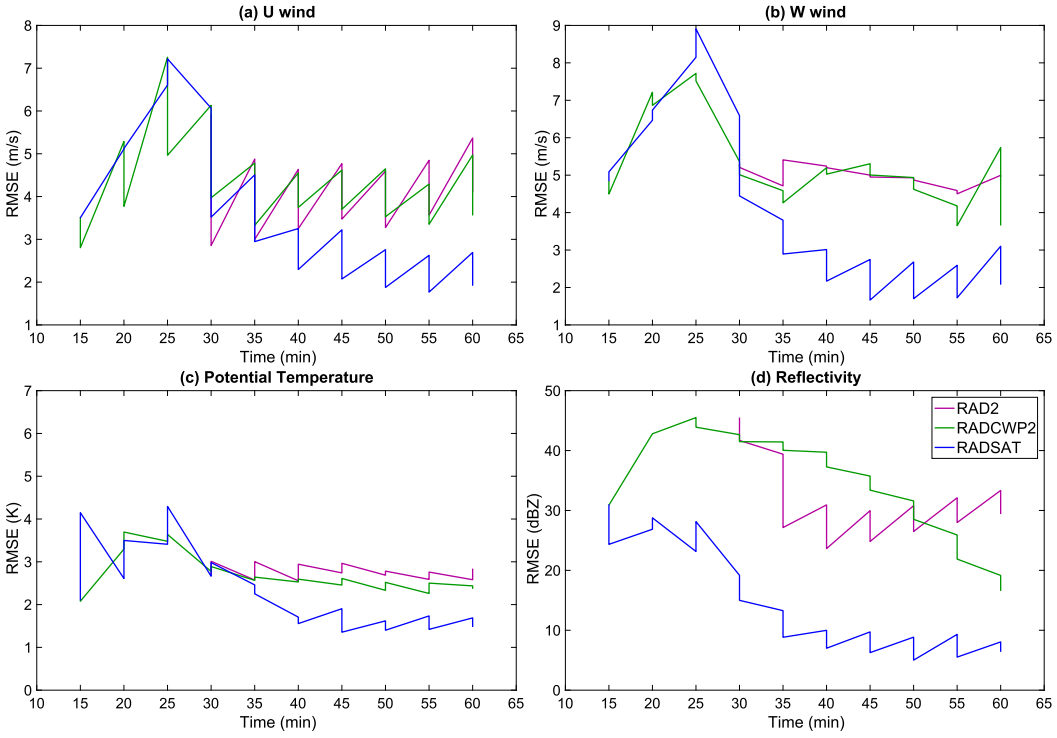

FIG. 11. As in Fig. 7, but for experiments RAD2 (purple), RADCWP2 (green), and RADSAT (blue).

seen in the truth run. Slightly weak and discontinuous reflectivity patterns extending to the east boundary indicate an incorrect analysis of the cirrus outflow. For RADCWP2, the analysis looks much better than found when assimilating only radar data, especially the extent of the 20-dBZ reflectivity region, which is close to that seen in the truth run. The supercell (Fig. 8d) as indicated by the maximum vorticity and reflectivity values corresponds well with the truth simulation. However, much stronger reflectivities and chaotic vorticity patterns are displayed in both the horizontal and vertical sections. Both the left- and right-moving cells look too strong because the maximum vorticity reaches $>1800 \times 10^{-5}\,\mathrm{s}^{-1}$, or over $200 \times 10^{-5}\,\mathrm{s}^{-1}$ greater than that seen in the truth simulation (Fig. 5a). When TPW data are also assimilated in the experiment RADSAT, the precipitating area is approximately identical in shape and coverage compared with the truth run (Figs. 8e,f), although the vorticity field somehow still has noise patterns inside the storm. But we notice that the maximum vertical velocity and relative vorticity are enhanced. The analyses for the water vapor mixing ratio at the end of the DA cycles for RAD2 and RADCWP2 (Figs. 9c–f) are much less than those in the truth simulation (Figs. 9a,b). But this dry bias in the water vapor mixing ratios is largely corrected with additional assimilation of TPW data (Figs. 9g,h). This result illustrates that a storm environment dry bias cannot be corrected by assimilating radar data and satellite CWP data alone. Since the storm environment is fundamentally important for predicting the correct evolution of deep convection, the additional assimilation of TPW data can be very valuable.

The midlevel and near-surface temperature fields again show that assimilating only radar data generates the worst analysis among the RAD2, RADCWP2, and RADSAT experiments (Fig. 10). The representations of cold pools (Fig. 10c) and warm cores (Fig. 10d) embedded in the storm are hard to discern in RAD2. The temperature structure is improved in RADCWP2 (Figs. 10e,f), since the cold pool can be found to be associated with each of the storms, but it is too cold and some splitting cold areas are not expected. Comparing Figs. 10g,h with the others, we can find that the analyses with TPW data are the best among all the experiments as a result of the improved magnitude and location of the cold pool and the warm core structures.

Figure 11 shows the RMSE of four selected variables (horizontal wind u, vertical wind w, potential temperature pt, and reflectivity rf) for this second group of experiments. Results indicate assimilating CWP data prior to assimilating radar data does not alter the RMSEs very much. However, assimilating extra TPW reduces the u and w RMSEs compared to the other experiments, highlighting the importance of the near-storm environment. The

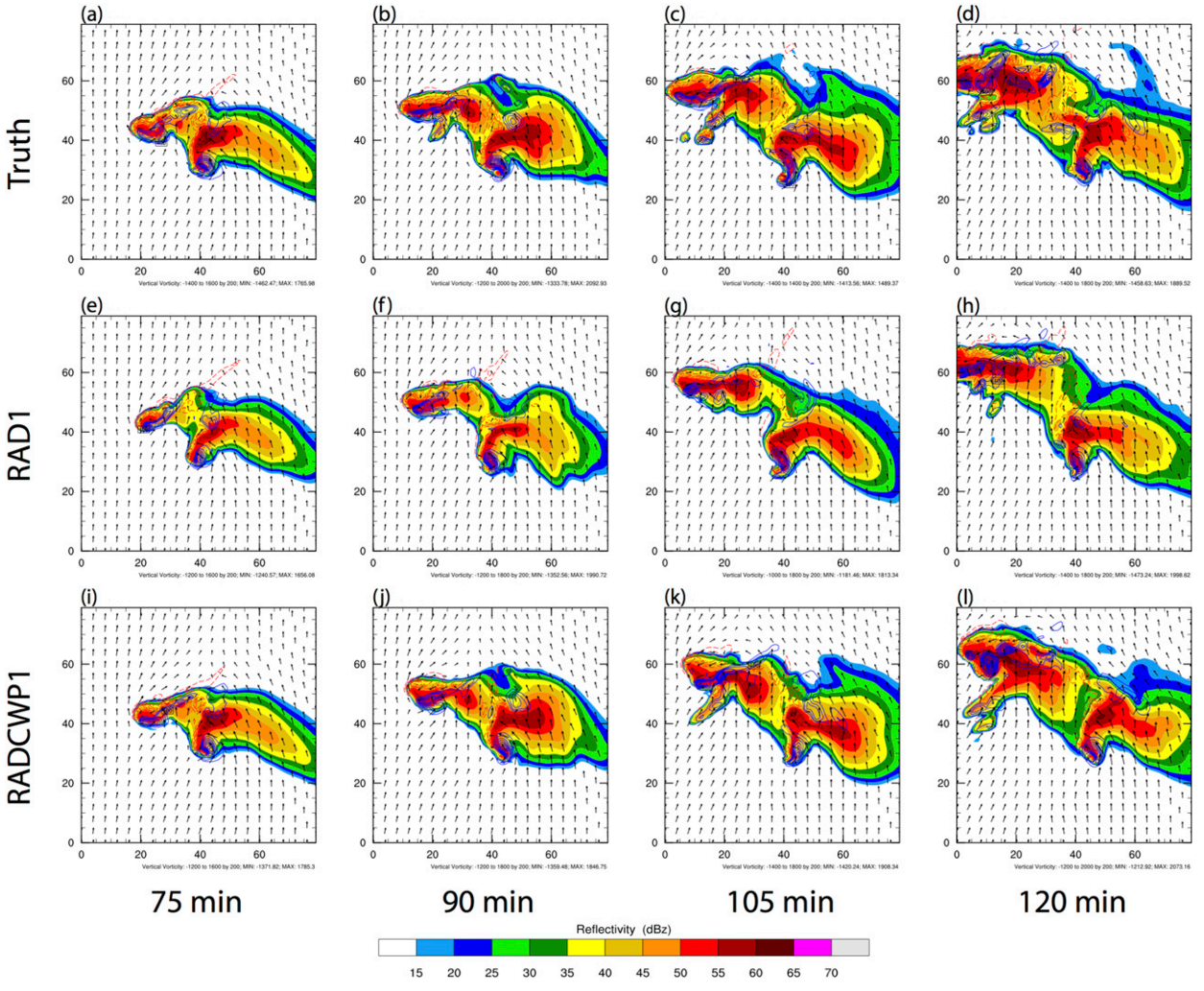

FIG. 12. The 4-km AGL wind, vorticity, and reflectivity from (a)–(d) truth, (e)–(h) RAD1, and (i)–(l) RADCWP1 at 15-min intervals for the 1-h free forecast initiated at 60 min.

errors of the wind and temperature in RADSAT are comparable to those drawn from the RAD2 and RADCWP2 experiments initially, but then they decrease once the radar data are assimilated, and finally they become the smallest among these three experiments. The error of the reflectivity is always lower than other experiments. Overall, the accuracy of the analysis improves when TPW data are assimilated. Further impacts of assimilating TPW data are shown in the forecast evaluation section.

5. Forecast verification

a. Experiments with perfect storm environment

To evaluate the impact of assimilating different data for short-term forecasts, a 1-h free forecast is launched. The reflectivity fields at 4 km AGL from the DA experiments are compared to the truth simulation. In general, all the prognostic variables are appropriately predicted in the forecasts. The forecasts of RAD1 (Figs. 12e–h) generate slightly smaller areas covered by >55-dBZ reflectivity compared to those of the truth (Figs. 12a–d) and RADCWP1 (Figs. 12i–l). However, assimilating CWP data together with radar data results in a small eastward displacement of the maximum vorticity in the forecasts.

Figure 13 shows the bias and RMSE for the 1-h forecast of the control member with and without assimilating CWP data. It shows that the biases for all selected variables are improved (closer to zero) when CWP data are assimilated (Figs. 13a,c,e,g). The RMSEs in RADCWP1 are smaller for most of the forecast period. But they are greater than the RMSEs in RAD1 after 50 min for the u wind component, and after 40 min for vertical velocity and potential temperature. At the

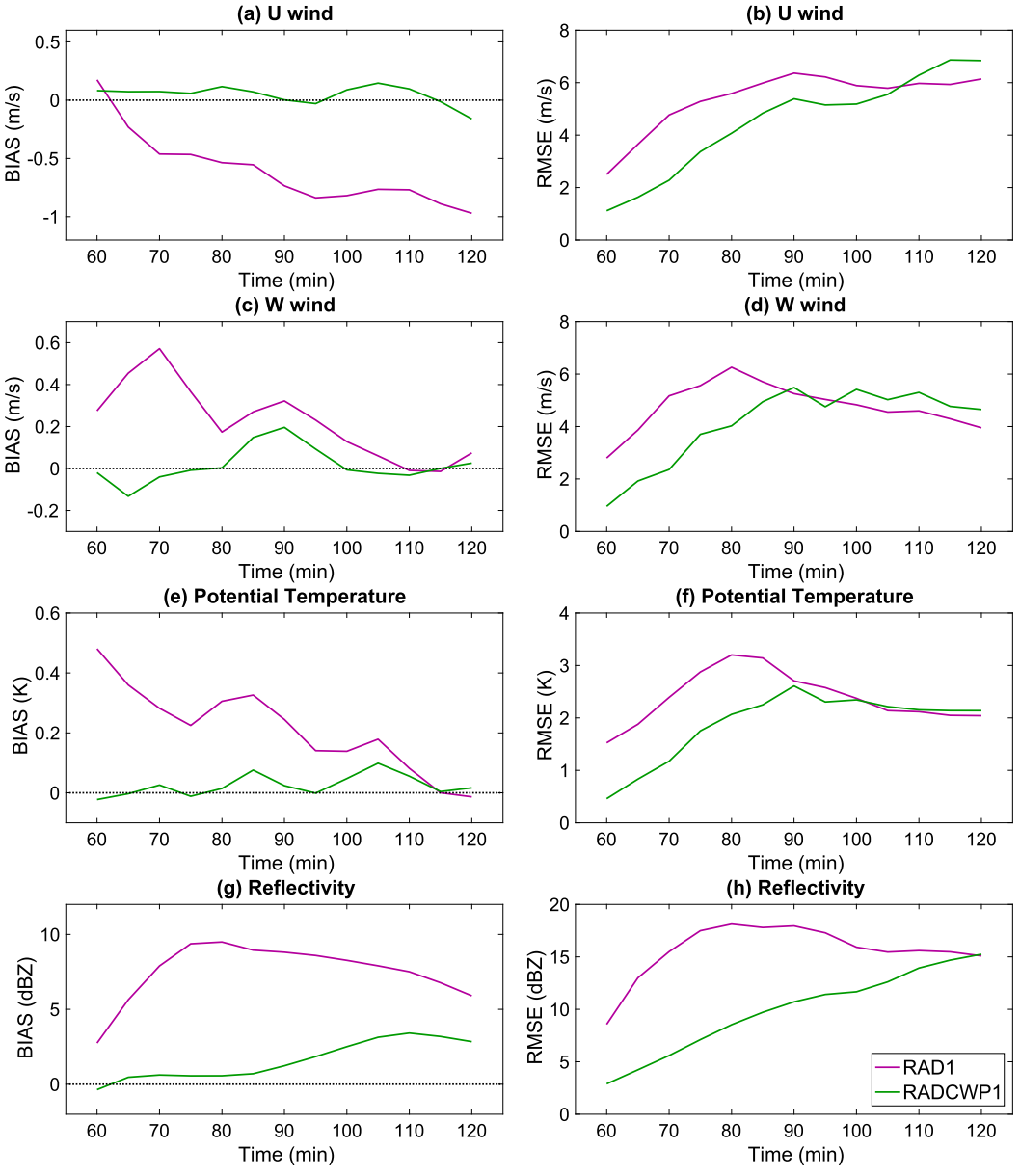

FIG. 13. (left) Bias and (right) RMSE of the 1-h free forecast initiated at 60 min of model time for RAD1 (purple) and RADCWP1 (green) for (a),(b) u ($\mathrm{m\,s^{-1}}$); (c),(d) w ($\mathrm{m\,s^{-1}}$); (e),(f) pt(K); and (g),(h) simulated rf(dBZ).

end of the forecast period, RMSEs for nearly all variables are very close to each other, especially for potential temperature and reflectivity.

To further quantify the impact of the radar and satellite data, in addition to statistical errors, the following skill scores are calculated: probability of detection (POD), false alarm rate (FAR), critical success index (CSI), and Heidke skill score (HSS). A threshold of 40 dBZ for reflectivity is used as the threshold for all skill scores (Table 2). A good forecast should maximize the number of "hits" leading to a high POD with low FAR as a consequence of suppressing false alarms.

A set of skill scores between simulated reflectivity fields obtained by the truth run and each experiment over the whole domain is shown in Fig. 14. RAD1 and

TABLE 2. Contingency table for accumulating hits, false alarms, misses, and correct null forecasts.

Contingency table		Event observed (>40 dBZ) Yes	No
Event forecast (>40 dBZ)	Yes	Hits	False alarms
	No	Misses	Null forecasts

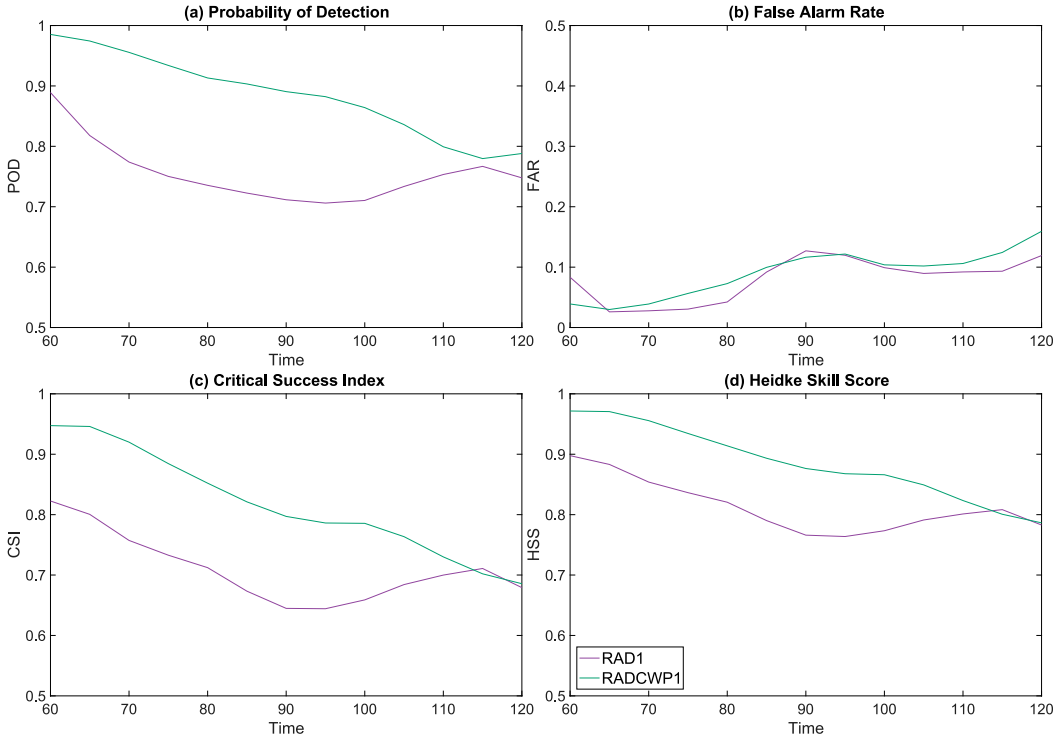

FIG. 14. Skill scores, including (a) POD, (b) FAR, (c) CSI, and (d) HSS, of the 1-h free forecast initiated at 60 min of model time for RAD1 (purple) and RADCWP1 (green).

RADCWP1 generate similar FAR, but the former has a slightly lower FAR than RADCWP1. Since RADCWP1 combines CWP data containing nonprecipitating cloud properties, such as cloud water and cloud ice, and spreads this information in space and to different variables through flow-dependent covariances, RADCWP1 generates a higher POD than RAD1 during the forecast period, resulting in a higher CSI and HSS. The differences in CSI and HSS between the two experiments decrease with time, and they become very small at 115 min. However, RADCWP1 continually has higher overall skill scores for the first 50 min of the forecast.

b. Experiments with dry bias in storm environment

Similar to the last section, the impact of various data on the short time forecast started from an imperfect storm environment with a dry bias is investigated. Obviously, the very weak initialized storm cell in RAD2 after 30 min of DA cycles quickly dies once the forecast is launched (Figs. 15a–d). Though the major right-moving storm is much better initialized in RADCWP2 when CWP are also assimilated, it also dies at roughly 30 min of the forecast (Figs. 15e–h). The reason for the quick dissipation of the storm is simple: the storm environment is not correctly generated by DA even when both radar data and CWP data are assimilated. When TPW data are also assimilated into the RADSAT experiment, the storm environment is corrected to some extent, enough that the two storm cells are reproduced in the right time. The left-splitting storm, which is not produced in previous experiments, is partly captured by RADSAT because more adequate low-level moisture and thus a more accurate environmental instability are produced by the DA. Though the intensity and area of these two storm cells are generally well maintained during the 60-min forecast period (Figs. 15i–l), the left-splitting storm has a northwest bias during the 1-h forecast period.

The bias and RMSE for four variables are calculated for the experiments within the biased environment and shown in Fig. 16. These clearly demonstrate that errors of zonal wind, potential temperature, and reflectivity can be significantly reduced when TPW data are assimilated (Figs. 16a,b,e–h). Though the bias of the vertical wind field (Fig. 16c) is the best in the RADSAT experiment, the results of RMSE look mixed for the vertical wind field (Fig. 16d). Finally, the same set of skill scores that compared RAD2, RADCWP2, and RADSAT with the truth simulation are plotted in Fig. 17. RAD2 essentially has no skill for all forecast times, while RADCWP2 shows some skill out to a 30-min forecast but almost no skill thereafter. RADSAT generates higher skill scores than either RAD2 or

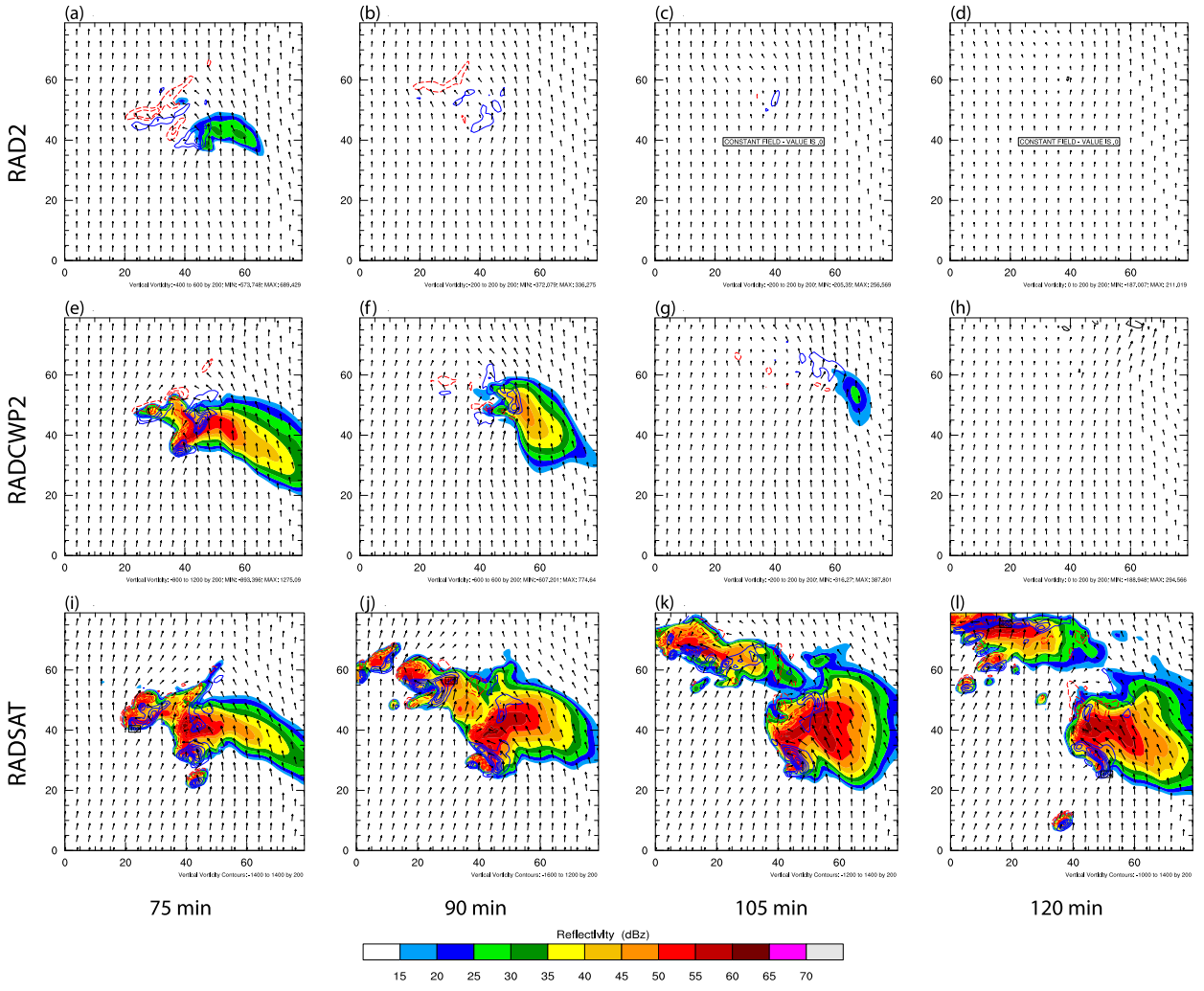

FIG. 15. As in Fig. 12, but for experiments RAD2, RADCWP2, and RADSAT.

RADCWP2. This result clearly indicates that incorporating TPW data for correcting moisture values within the storm environment is very helpful, even if using vertically integrated moisture data cannot precisely adjust the vertical moisture distribution of the storm environment.

6. Conclusions

In this study, synthetic radar radial velocity and reflectivity data, along with satellite CWP and TPW data, are assimilated into the WRF Model using the En3DVar system within an OSSE. Two groups of DA and forecast experiments are performed. The first set of experiments assimilates storm-resolving radar data and CWP data using a perfect storm environment, while a second group of experiments assimilate additional TPW data using a storm environment with a dry bias. The advantages of simultaneously assimilating both radar and satellite data, as well as the importance of an accurate storm environment, are shown by comparing analyses and forecasts against the reference truth run.

The results from the first set of experiments indicate that assimilating satellite-derived CWP data reduces the spinup time for convection within the model compared to assimilating only radar data. When assimilating only radar radial velocity and reflectivity data, the wind analysis is very close to the truth run, but there are errors in the analyses of temperature and nonprecipitating hydrometeors, as these variables are not directly observed by radars. The additional satellite-derived CWP data do provide information on nonprecipitating hydrometeors, and these data can be assimilated before precipitating clouds are generated. The RAD1 experiment underestimates the cold pool strength, which is an important characteristic of any storm, but it still

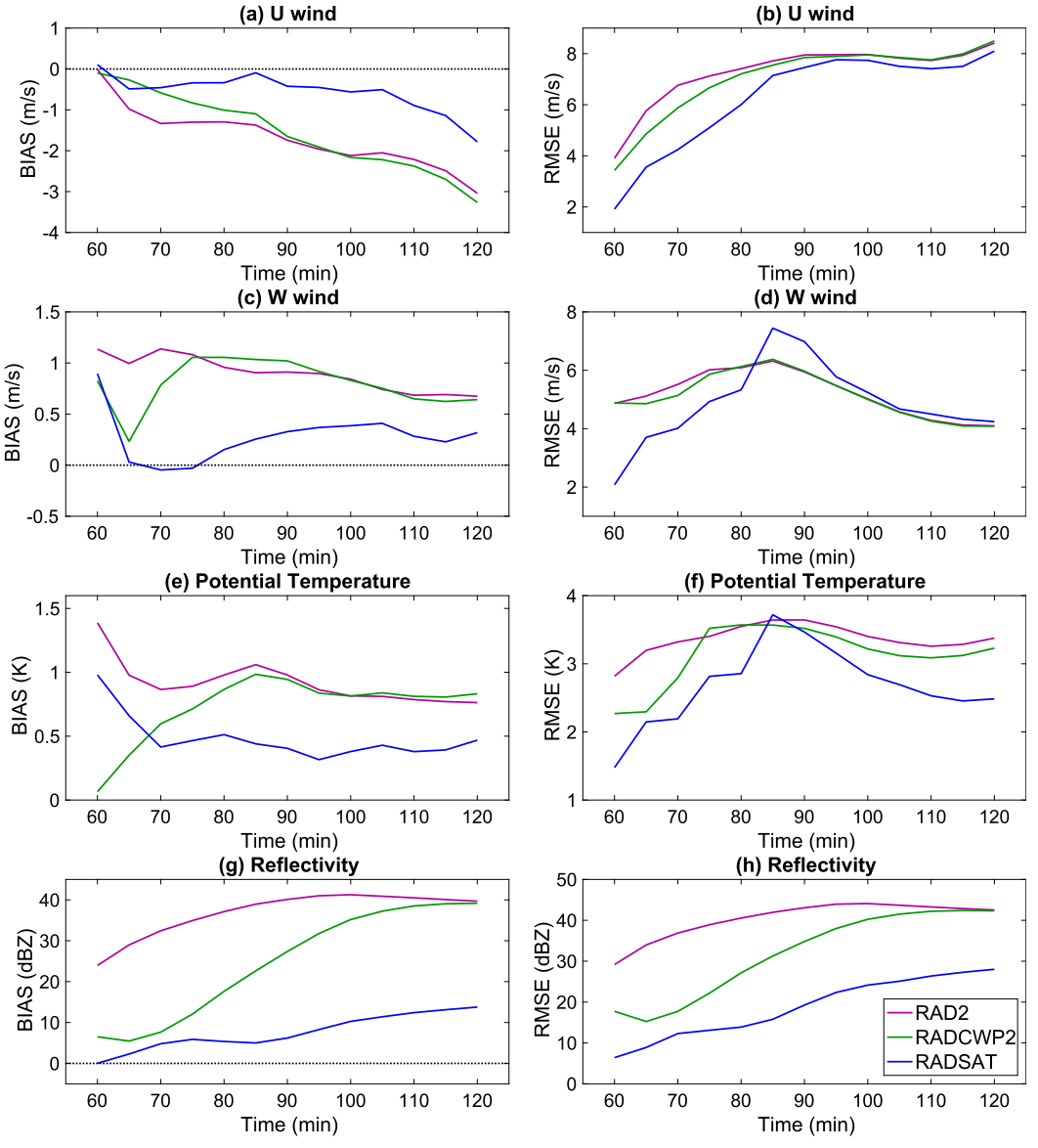

FIG. 16. As in Fig. 13, but for experiments RAD2 (purple), RADCWP2 (green), and RADSAT (blue).

produces an acceptable 1-h forecast, though with larger biases in magnitude and storm location than found in RADCWP1. For the forecast in RADCWP1, the errors are actually reduced by a factor of 2 and PODs are increased by 0.2 during the first 45-min forecast period compared to RAD1. The combination of CWP and radar data produces a more accurate analysis and forecast when using a perfect storm environment.

The second group of experiments examines the performance of radar and satellite DA when the storm environment has a dry bias, and seeks to determine whether assimilating TPW data can help improve the biased storm environment. The biased environment has reduced moisture content in the troposphere, such that the atmosphere becomes too stable to trigger and sustain convection. Assimilating only radar data does not generate sustained convection, since radar data contain little information about atmospheric moisture and are unable to adjust the environment. Much better analyses and forecasts are produced by also assimilating CWP data in the RADCWP2 experiment. The right-splitting storm survives much longer, up to 45 min in the forecast, but it still has a motion bias to the northeast of the reference truth. In addition, the left-moving storm is still not analyzed. This is because the CWP data contain cloud information but not water vapor information.

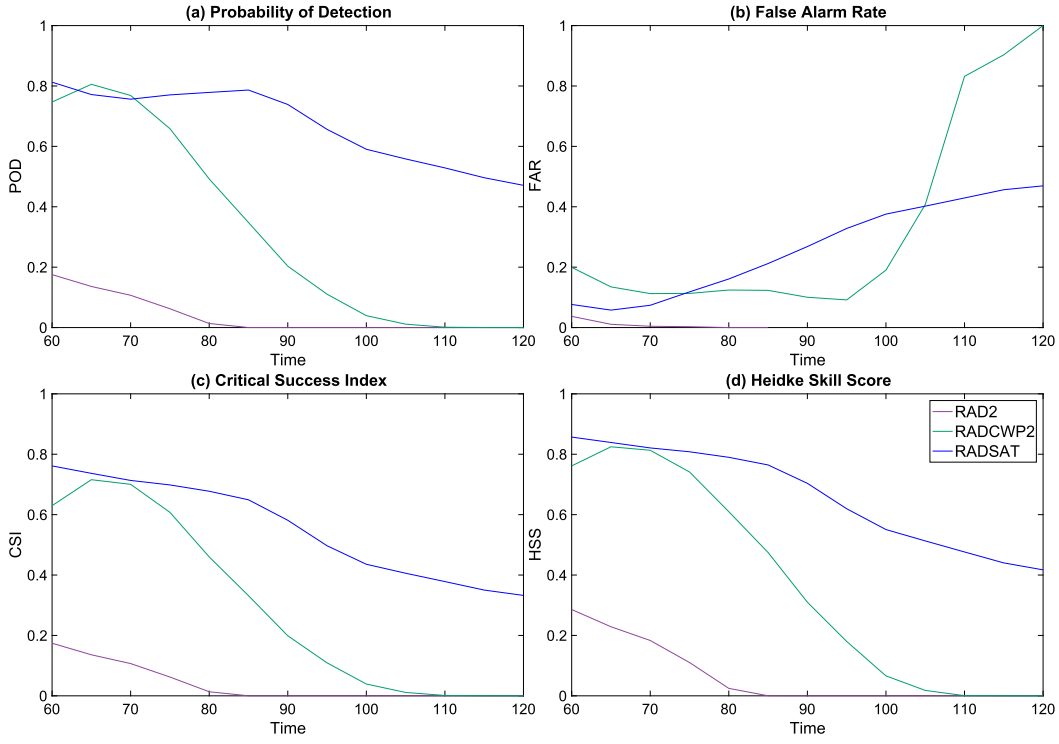

FIG. 17. As in Fig. 14, but for experiments RAD2 (purple), RADCWP2 (green), and RADSAT (blue).

Thus, CWP may help correct the dry bias in the storm environment slightly, but its information content is too small to make a dramatic improvement. Some positive impacts of assimilating TPW are observed in both the analysis and forecast because TPW data contain information on the total moisture in the troposphere. Although the left-splitting storm has a northwestern bias, the analysis of the two storms is more accurately depicted in magnitude and location by the end of the DA period compared with the experiment, which assimilates only radar data or both radar and CWP data. Higher POD and HSS than the other experiments suggest that TPW data are helpful in correcting a dry bias in the storm environment. This group of experiments emphasize that the storm environment, especially the moisture profile, is fundamentally important to the storm development. Assimilating radar data is important because these data can resolve the internal storm structure. However, the storm environment is also important and can be adjusted and improved by assimilating other observations, such as satellite TPW data.

In this study, although some encouraging results are obtained from assimilation of combined CWP data and radar data into a convective-scale model in OSSEs, further investigation of assimilating satellite data together with radar data is needed. Research is ongoing for using new products from the GOES-R ABI in DA, and it is expected that the high-resolution satellite data from this new instrument will be very helpful in constructing internal storm structures and in providing information on the storm environment so that convective-scale NWP can be improved in the future.

Acknowledgments. This research was funded by the NOAA Warn-on-Forecast project provided by NOAA/Office of Oceanic and Atmospheric Research under NOAA–University of Oklahoma Cooperative Agreement NA11OAR4320072, U.S. Department of Commerce; and NSF Grants AGS-1341878 and AGS-1359703. The NOAA Research and Development High Performance Computing Program and the OSCER from the University of Oklahoma are acknowledged for providing computing and storage resources.

REFERENCES

Adlerman, E. J., and K. K. Droegemeier, 2002: The sensitivity of numerically simulated cyclic mesocyclogenesis to variations in model physical and computational parameters. *Mon. Wea. Rev.*, **130**, 2671–2691, https://doi.org/10.1175/1520-0493(2002)130<2671:TSONSC>2.0.CO;2.

Aksoy, A., D. C. Dowell, and C. Snyder, 2009: A multicase comparative assessment of the ensemble Kalman filter for assimilation of radar observations. Part I: Storm-scale analyses. *Mon. Wea. Rev.*, **137**, 1805–1824, https://doi.org/10.1175/2008MWR2691.1.

Anderson, J., T. Hoar, K. Raeder, H. Liu, N. Collins, R. Torn, and A. Avellano, 2009: The Data Assimilation Research Testbed: A community facility. *Bull. Amer. Meteor. Soc.*, **90**, 1283–1296, https://doi.org/10.1175/2009BAMS2618.1.

Berre, L., O. Pannekoucke, G. Desroziers, S. Ştefănescu, B. Chapnik, and L. Raynaud, 2007: A variational assimilation ensemble and the spatial filtering of its error covariances: Increase of sample size by local spatial averaging. *Proc. ECMWF Workshop on Flow-Dependent Aspects of Data Assimilation*, Reading, United Kingdom, ECMWF, 151–168.

Bonavita, M., L. Isaksen, and E. Holm, 2012: On the use of EDA background error variances in the ECMWF 4D-Var. *Quart. J. Roy. Meteor. Soc.*, **138**, 1540–1559, https://doi.org/10.1002/qj.1899.

Chen, Y., H. Wang, J. Min, X.-Y. Huang, P. Minnis, R. Zhang, J. Haggerty, and R. Palikonda, 2015: Variational assimilation of cloud liquid/ice water path and its impact on NWP. *J. Appl. Meteor. Climatol.*, **54**, 1809–1825, https://doi.org/10.1175/JAMC-D-14-0243.1.

Courtier, P., 1997: Dual formulation of four-dimensional variational assimilation. *Quart. J. Roy. Meteor. Soc.*, **123**, 2449–2461, https://doi.org/10.1002/qj.49712354414.

Crum, T. D., R. L. Alberty, and D. W. Burgess, 1993: Recording, archiving, and using WSR-88D data. *Bull. Amer. Meteor. Soc.*, **74**, 645–653, https://doi.org/10.1175/1520-0477(1993)074<0645:RAAUWD>2.0.CO;2.

Derber, J. C., and A. Rosati, 1989: A global oceanic data assimilation system. *J. Phys. Oceanogr.*, **19**, 1333–1347, https://doi.org/10.1175/1520-0485(1989)019<1333:AGODAS>2.0.CO;2.

——, and W. S. Wu, 1998: The use of TOVS cloud-cleared radiances in the NCEP SSI analysis system. *Mon. Wea. Rev.*, **126**, 2287–2299, https://doi.org/10.1175/1520-0493(1998)126<2287:TUOTCC>2.0.CO;2.

Dowell, D. C., F. Q. Zhang, L. J. Wicker, C. Snyder, and N. A. Crook, 2004: Wind and temperature retrievals in the 17 May 1981 Arcadia, Oklahoma, supercell: Ensemble Kalman filter experiments. *Mon. Wea. Rev.*, **132**, 1982–2005, https://doi.org/10.1175/1520-0493(2004)132<1982:WATRIT>2.0.CO;2.

——, L. J. Wicker, and C. Snyder, 2011: Ensemble Kalman Filter assimilation of radar observations of the 8 May 2003 Oklahoma City supercell: Influences of reflectivity observations on storm-scale analyses. *Mon. Wea. Rev.*, **139**, 272–294, https://doi.org/10.1175/2010MWR3438.1.

Gao, J., and D. J. Stensrud, 2012: Assimilation of reflectivity data in a convective-scale, cycled 3DVAR framework with hydrometeor classification. *J. Atmos. Sci.*, **69**, 1054–1065, https://doi.org/10.1175/JAS-D-11-0162.1.

——, and ——, 2014: Some observing system simulation experiments with a hybrid 3DEnVAR system for storm-scale radar data assimilation. *Mon. Wea. Rev.*, **142**, 3326–3346, https://doi.org/10.1175/MWR-D-14-00025.1.

——, M. Xue, K. Brewster, and K. K. Droegemeier, 2004: A three-dimensional variational data analysis method with recursive filter for Doppler radars. *J. Atmos. Oceanic Technol.*, **21**, 457–469, https://doi.org/10.1175/1520-0426(2004)021<0457:ATVDAM>2.0.CO;2.

——, and Coauthors, 2013: A real-time weather-adaptive 3DVAR analysis system for severe weather detections and warnings. *Wea. Forecasting*, **28**, 727–745, https://doi.org/10.1175/WAF-D-12-00093.1.

——, C. H. Fu, D. J. Stensrud, and J. S. Kain, 2016: OSSEs for an ensemble 3DVAR data assimilation system with radar observations of convective storms. *J. Atmos. Sci.*, **73**, 2403–2426, https://doi.org/10.1175/JAS-D-15-0311.1.

Harris, B. A., and G. Kelly, 2001: A satellite radiance-bias correction scheme for data assimilation. *Quart. J. Roy. Meteor. Soc.*, **127**, 1453–1468, https://doi.org/10.1002/qj.49712757418.

Houtekamer, P. L., and H. L. Mitchell, 1998: Data assimilation using an ensemble Kalman filter technique. *Mon. Wea. Rev.*, **126**, 796–811, https://doi.org/10.1175/1520-0493(1998)126<0796:DAUAEK>2.0.CO;2.

Johnson, A., and X. Wang, 2017: Design and implementation of a GSI-based convection-allowing ensemble data assimilation and forecast system for the PECAN field experiment. Part I: Optimal configurations for nocturnal convection prediction using retrospective cases. *Wea. Forecasting*, **32**, 289–315, https://doi.org/10.1175/WAF-D-16-0102.1.

——, ——, J. Carely, L. Wicker, and C. Karstens, 2015: A comparison of multiscale GSI-based EnKF and 3DVar data assimilation using radar and conventional observations for midlatitude convective-scale precipitation forecasts. *Mon. Wea. Rev.*, **143**, 3087–3108, https://doi.org/10.1175/MWR-D-14-00345.1.

Jones, T. A., and D. J. Stensrud, 2012: Assimilating AIRS temperature and mixing ratio profiles using an ensemble Kalman filter approach for convective-scale forecasts. *Wea. Forecasting*, **27**, 541–564, https://doi.org/10.1175/WAF-D-11-00090.1.

——, ——, P. Minnis, and R. Palikonda, 2013: Evaluation of a forward operator to assimilate cloud water path into WRF-DART. *Mon. Wea. Rev.*, **141**, 2272–2289, https://doi.org/10.1175/MWR-D-12-00238.1.

——, ——, L. Wicker, P. Minnis, and R. Palikonda, 2015: Simultaneous radar and satellite data storm-scale assimilation using an ensemble Kalman filter approach for 24 May 2011. *Mon. Wea. Rev.*, **143**, 165–194, https://doi.org/10.1175/MWR-D-14-00180.1.

——, K. Knopfmeier, D. Wheatley, G. Creager, P. Minnis, and R. Palikonda, 2016: Storm-scale data assimilation and ensemble forecasting with the NSSL experimental Warn-on-Forecast system. Part II: Combined radar and satellite data experiments. *Wea. Forecasting*, **31**, 297–327, https://doi.org/10.1175/WAF-D-15-0107.1.

Kuo, Y. H., X. Zou, and Y. R. Guo, 1996: Variational assimilation of precipitable water using a nonhydrostatic mesoscale adjoint model. Part I: Moisture retrieval and sensitivity experiments. *Mon. Wea. Rev.*, **124**, 122–147, https://doi.org/10.1175/1520-0493(1996)124<0122:VAOPWU>2.0.CO;2.

Li, J., T. J. Schmit, X. Jin, and G. Martin, 2010: GOES-R Advanced Baseline Imager (ABI) algorithm theoretical basis document for legacy atmospheric moisture profile, legacy atmospheric temperature profile, total precipitable water, and derived atmospheric stability indices. Version 2.0, NOAA/NESDIS/STAR, 106 pp.

Lorenc, A. C., 2003: The potential of the ensemble Kalman filter for NWP—A comparison with 4D-Var. *Quart. J. Roy. Meteor. Soc.*, **129**, 3183–3203, https://doi.org/10.1256/qj.02.132.

Matricardi, M., F. Chevallier, G. Kelly, and J. N. Thepaut, 2004: An improved general fast radiative transfer model for the assimilation of radiance observations. *Quart. J. Roy. Meteor. Soc.*, **130**, 153–173, https://doi.org/10.1256/qj.02.181.

Migliorini, S., 2012: On the equivalence between radiance and retrieval assimilation. *Mon. Wea. Rev.*, **140**, 258–265, https://doi.org/10.1175/MWR-D-10-05047.1.

Minnis, P., and Coauthors, 2008a: Cloud detection in nonpolar regions for CERES using TRMM VIRS and Terra and Aqua MODIS data. *IEEE Trans. Geosci. Remote Sens.*, **46**, 3857–3884, https://doi.org/10.1109/TGRS.2008.2001351.

——, and Coauthors, 2008b: Near-real time cloud retrievals from operational and research meteorological satellites. *Remote*

Sensing of Clouds and the Atmosphere XIII, R. H. Picard et al., Eds., Society of Photo-Optical Instrumentation Engineers (SPIE Proceedings, Vol. 7107), 710703, https://doi.org/10.1117/12.800344.

——, and Coauthors, 2011: CERES Edition-2 cloud property retrievals using TRMM VIRS and Terra and Aqua MODIS data—Part I: Algorithms. *IEEE Trans. Geosci. Remote Sens.*, **49**, 4374–4400, https://doi.org/10.1109/TGRS.2011.2144601.

Noda, A., and H. Niino, 2003: Critical grid size for simulating convective storms: A case study of the Del City supercell storm. *Geophys. Res. Lett.*, **30**, 1844, https://doi.org/10.1029/2003gl017498.

Okamoto, K., A. P. McNally, and W. Bell, 2014: Progress towards the assimilation of all-sky infrared radiances: An evaluation of cloud effects. *Quart. J. Roy. Meteor. Soc.*, **140**, 1603–1614, https://doi.org/10.1002/qj.2242.

Pavelin, E. G., S. J. English, and J. R. Eyre, 2008: The assimilation of cloud-affected infrared satellite radiances for numerical weather prediction. *Quart. J. Roy. Meteor. Soc.*, **134**, 737–749, https://doi.org/10.1002/qj.243.

Polkinghorne, R., and T. Vukicevic, 2011: Data assimilation of cloud-affected radiances in a cloud-resolving model. *Mon. Wea. Rev.*, **139**, 755–773, https://doi.org/10.1175/2010MWR3360.1.

——, ——, and K. F. Evans, 2010: Validation of cloud-resolving model background data for cloud data assimilation. *Mon. Wea. Rev.*, **138**, 781–795, https://doi.org/10.1175/2009MWR3012.1.

Prates, C., S. Migliorini, S. English, and E. Pavelin, 2014: Assimilation of satellite infrared sounding measurements in the presence of heterogeneous cloud fields. *Quart. J. Roy. Meteor. Soc.*, **140**, 2062–2077, https://doi.org/10.1002/qj.2279.

Rotunno, R., and J. Klemp, 1985: On the rotation and propagation of simulated supercell thunderstorms. *J. Atmos. Sci.*, **42**, 271–292, https://doi.org/10.1175/1520-0469(1985)042<0271:OTRAPO>2.0.CO;2.

Saunders, R., M. Matricardi, and P. Brunel, 1999: An improved fast radiative transfer model for assimilation of satellite radiance observations. *Quart. J. Roy. Meteor. Soc.*, **125**, 1407–1425, https://doi.org/10.1002/qj.1999.49712555615.

Schoenberg Ferrier, B., 1994: A double-moment multiple-phase four-class bulk ice scheme. Part I: Description. *J. Atmos. Sci.*, **51**, 249–280, https://doi.org/10.1175/1520-0469(1994)051<0249:ADMMPF>2.0.CO;2.

Smith, P. L., C. G. Myers, and H. D. Orville, 1975: Radar reflectivity factor calculations in numerical cloud models using bulk parameterization of precipitation. *J. Appl. Meteor.*, **14**, 1156–1165, https://doi.org/10.1175/1520-0450(1975)014<1156:RRFCIN>2.0.CO;2.

Stengel, M., M. Lindskog, P. Unden, and N. Gustafsson, 2013: The impact of cloud-affected IR radiances on forecast accuracy of a limited-area NWP model. *Quart. J. Roy. Meteor. Soc.*, **139**, 2081–2096, https://doi.org/10.1002/qj.2102.

Stensrud, D. J., and J. D. Gao, 2010: Importance of horizontally inhomogeneous environmental initial conditions to ensemble storm-scale radar data assimilation and very short-range forecasts. *Mon. Wea. Rev.*, **138**, 1250–1272, https://doi.org/10.1175/2009MWR3027.1.

——, and Coauthors, 2009: Convective-scale warn-on-forecast system: A vision for 2020. *Bull. Amer. Meteor. Soc.*, **90**, 1487, https://doi.org/10.1175/2009BAMS2795.1.

Sun, J. Z., 2005: Initialization and numerical forecasting of a supercell storm observed during STEPS. *Mon. Wea. Rev.*, **133**, 793–813, https://doi.org/10.1175/MWR2887.1.

Vukicevic, T., T. Greenwald, M. Zupanski, D. Zupanski, T. Vonder Haar, and A. S. Jones, 2004: Mesoscale cloud state estimation from visible and infrared satellite radiances. *Mon. Wea. Rev.*, **132**, 3066–3077, https://doi.org/10.1175/MWR2837.1.

——, M. Sengupta, A. S. Jones, and T. Vonder Haar, 2006: Cloud-resolving satellite data assimilation: Information content of IR window observations and uncertainties in estimation. *J. Atmos. Sci.*, **63**, 901–919, https://doi.org/10.1175/JAS3639.1.

Wang, X., D. M. Barker, C. Snyder, and T. M. Hamill, 2008: A hybrid ETKF–3DVAR data assimilation scheme for the WRF model. Part I: Observing system simulation experiment. *Mon. Wea. Rev.*, **136**, 5116–5131, https://doi.org/10.1175/2008MWR2444.1.

Wang, Y., and X. Wang, 2017: Direct assimilation of radar reflectivity without tangent linear and adjoint of the nonlinear observation operator in the GSI-based EnVar system: Methodology and experiment with the 8 May 2003 Oklahoma City tornadic supercell. *Mon. Wea. Rev.*, **145**, 1447–1471, https://doi.org/10.1175/MWR-D-16-0231.1.

Weisman, M. L., and J. B. Klemp, 1982: The dependence of numerically simulated convective storms on vertical wind shear and buoyancy. *Mon. Wea. Rev.*, **110**, 504–520, https://doi.org/10.1175/1520-0493(1982)110<0504:TDONSC>2.0.CO;2.

Weisz, E., J. Li, J. L. Li, D. K. Zhou, H.-L. Huang, M. D. Goldberg, and P. Yang, 2007: Cloudy sounding and cloud-top height retrieval from AIRS alone single field-of-view radiance measurements. *Geophys. Res. Lett.*, **34**, L12802, https://doi.org/10.1029/2007gl030219.

Weng, F. Z., 2007: Advances in radiative transfer modeling in support of satellite data assimilation. *J. Atmos. Sci.*, **64**, 3799–3807, https://doi.org/10.1175/2007JAS2112.1.

——, and Q. H. Liu, 2003: Satellite data assimilation in numerical weather prediction models. Part I: Forward radiative transfer and Jacobian modeling in cloudy atmospheres. *J. Atmos. Sci.*, **60**, 2633–2646, https://doi.org/10.1175/1520-0469(2003)060<2633:SDAINW>2.0.CO;2.

Wheatley, D. M., K. H. Knopfmeier, T. A. Jones, and G. J. Creager, 2015: Storm-scale data assimilation and ensemble forecasting with the NSSL experimental Warn-on-Forecast system. Part I: Radar data experiments. *Wea. Forecasting*, **30**, 1795–1817, https://doi.org/10.1175/WAF-D-15-0043.1.

Xu, Q., and L. Wei, 2013: Prognostic equation for radar radial velocity derived by considering atmospheric refraction and Earth curvature. *J. Atmos. Sci.*, **70**, 3328–3338, https://doi.org/10.1175/JAS-D-13-011.1.

——, H. Gu, and S. Yang, 2001: Simple adjoint method for three-dimensional wind retrievals from single-Doppler radar. *Quart. J. Roy. Meteor. Soc.*, **127**, 1053–1067, https://doi.org/10.1002/qj.49712757319.

Yussouf, N., and D. J. Stensrud, 2010: Impact of phased-array radar observations over a short assimilation period: Observing system simulation experiments using an ensemble Kalman filter. *Mon. Wea. Rev.*, **138**, 517–538, https://doi.org/10.1175/2009MWR2925.1.

——, E. R. Mansell, L. J. Wicker, D. M. Wheatley, and D. J. Stensrud, 2013: The ensemble Kalman filter analyses and forecasts of the 8 May 2003 Oklahoma City tornadic supercell storm using single- and double-moment microphysics schemes. *Mon. Wea. Rev.*, **141**, 3388–3412, https://doi.org/10.1175/MWR-D-12-00237.1.

Zhang, F., C. Snyder, and J. Sun, 2004: Impacts of initial estimate and observations on the convective-scale data assimilation with an ensemble Kalman filter. *Mon. Wea. Rev.*, **132**, 1238–1253, https://doi.org/10.1175/1520-0493(2004)132<1238:IOIEAO>2.0.CO;2.

Zupanski, D., S. Q. Zhang, M. Zupanski, A. Y. Hou, and S. H. Cheung, 2011: A prototype WRF-based ensemble data assimilation system for dynamically downscaling satellite precipitation observations. *J. Hydrometeor.*, **12**, 118–134, https://doi.org/10.1175/2010JHM1271.1.